Space Sci Rev (2010) 150: 81–124
DOI 10.1007/s11214-010-9634-2

Lunar Reconnaissance Orbiter Camera (LROC) Instrument Overview

M.S. Robinson · S.M. Brylow · M. Tschimmel · D. Humm · S.J. Lawrence · P.C. Thomas · B.W. Denevi · E. Bowman-Cisneros · J. Zerr · M.A. Ravine · M.A. Caplinger · F.T. Ghaemi · J.A. Schaffner · M.C. Malin · P. Mahanti · A. Bartels · J. Anderson · T.N. Tran · E.M. Eliason · A.S. McEwen · E. Turtle · B.L. Jolliff · H. Hiesinger

Received: 22 June 2009 / Accepted: 2 February 2010 / Published online: 11 March 2010

Abstract The Lunar Reconnaissance Orbiter Camera (LROC) Wide Angle Camera (WAC) and Narrow Angle Cameras (NACs) are on the NASA Lunar Reconnaissance Orbiter (LRO).

M.S. Robinson (✉) · M. Tschimmel · S.J. Lawrence · B.W. Denevi · E. Bowman-Cisneros · P. Mahanti · T.N. Tran
School of Earth and Space Exploration, Arizona State University, Tempe, AZ, USA
e-mail: mrobinson@ser.asu.edu

S.M. Brylow · J. Zerr · M.A. Ravine · M.A. Caplinger · J.A. Schaffner · M.C. Malin
Malin Space Science Systems, San Diego, CA, USA

D. Humm
Space Instrument Calibration Consulting, Annapolis, MD, USA

P.C. Thomas
Center for Radiophysics and Space Research, Cornell University, Ithaca, NY, USA

A. Bartels
National Aeronautics and Space Administration, Goddard Space Flight Center, Greenbelt, MD, USA

J. Anderson
Astrogeology Branch, United States Geological Survey, Flagstaff, AZ, USA

F.T. Ghaemi
Tony Ghaemi Optical Engineering, San Diego, CA, USA

E.M. Eliason · A.S. McEwen
Lunar and Planetary Lab, University of Arizona, Tucson, AZ, USA

E. Turtle
Applied Physics Lab, Johns Hopkins University, Laurel, MD, USA

B.L. Jolliff
Department of Earth and Planetary Sciences, Washington University, St. Louis, MO, USA

H. Hiesinger
Institut für Planetologie, Westfälische Wilhelms-Universität, Münster, Germany

The WAC is a 7-color push-frame camera (100 and 400 m/pixel visible and UV, respectively), while the two NACs are monochrome narrow-angle linescan imagers (0.5 m/pixel). The primary mission of LRO is to obtain measurements of the Moon that will enable future lunar human exploration. The overarching goals of the LROC investigation include landing site identification and certification, mapping of permanently polar shadowed and sunlit regions, meter-scale mapping of polar regions, global multispectral imaging, a global morphology base map, characterization of regolith properties, and determination of current impact hazards.

Keywords LRO · LROC · Instrument · Camera · Moon · Lunar · Calibration

1 Introduction

The observations, fieldwork, and sampling performed by the Apollo astronauts in lunar orbit and on the lunar surface yielded key insights into the origin, composition, and geologic evolution of the Moon and transformed humanity's knowledge of the Solar System. One of the key reasons that the Apollo missions were so successful was the intensive reconnaissance of the lunar surface performed using the five robotic Lunar Orbiter spacecraft, which provided synoptic photographic coverage of the entire Moon (Bowker and Hughes 1971), as well as high-resolution (1 m/pixel) observations specifically targeted at candidate Apollo landing sites. The Lunar Orbiter observations enabled the subsequent early Apollo landings and provided a valuable dataset for lunar geologic studies (El-Baz and Kosofsky 1970; Musgrove 1971). Existing lunar datasets (including Lunar Orbiter, Apollo, Clementine, and Lunar Prospector) are insufficient to effectively plan for future landings (human or robotic), especially in areas outside of the so-called "Apollo Zone" where meter-scale imagery and topographical data vital for landing site certification and operational planning is sparse or non-existent. Recent lunar missions (including JAXA's Kaguya mission, the CNSA Chang'E, and the ISRO's Chandrayaan-1) collected datasets of high scientific and exploration value, though none reveal lunar surface morphology at the scale needed to support the projected engineering requirements of NASA's next-generation human lunar exploration.

The Space Exploration Policy of the United States calls for a resumption of human lunar landings no later than 2020 under the aegis of Project Constellation, with the goal of eventually establishing a permanent outpost on the lunar surface (NASA 2004a). The Lunar Reconnaissance Orbiter (LRO) is designed to serve Project Constellation as Lunar Orbiter served Apollo, providing comprehensive remote sensing data that will enable the next generation of human lunar exploration and development. The Lunar Reconnaissance Orbiter Camera (LROC) is designed to address two of the LRO Level 1 measurement objectives: Landing site certification and determination of polar illumination (Chin et al. 2007; NASA 2004b). LROC data will help us redefine our understanding of the Moon's history and current state and guide lunar surface operations for decades to come.

LROC consists of three imaging subsystems (Figs. 1, 2, 5) with a supporting Sequence and Compressor System (SCS). The two Narrow Angle Cameras (NACs) are monochrome push-broom scanners, with an instantaneous field-of-view (IFOV) of 10-microradians (50-cm angular resolution from the nominal 50-km orbit (Fig. 2)). The multispectral Wide Angle Camera (WAC) is a push-frame imager with five visible wavelength filters (415 to 690 nm) with an IFOV of 1.498-milliradians (75-m angular size of pixel projected on the surface from a 50-km altitude) with the visible light filters, and IFOV of 9.672-milliradians

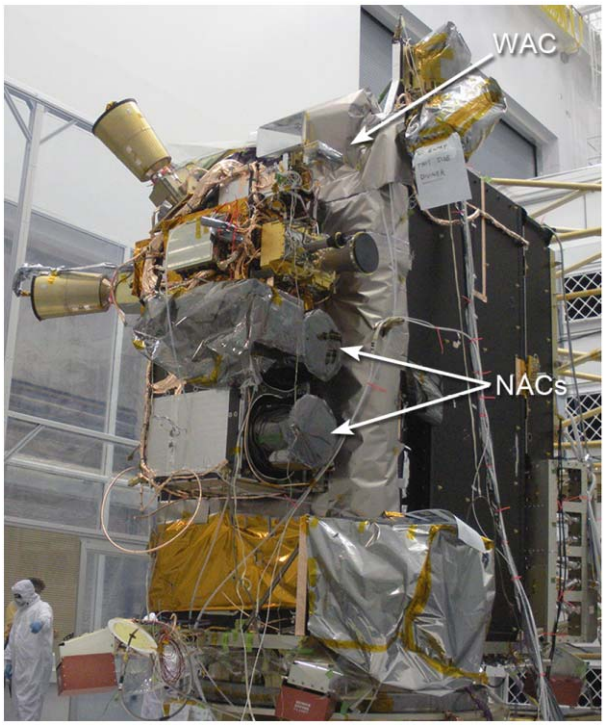

Fig. 1 The Lunar Reconnaissance Orbiter, with the positions of the two LROC Narrow Angle Cameras [NACs] and the Wide Angle Camera [WAC] highlighted (Image Credit: A. Bartels, NASA Goddard Space Flight Center)

(384-m angular size of pixel projected on the surface from a 50-km orbit) from two UV filters (320 and 360 nm). In addition to multispectral imaging, the WAC can operate in monochrome mode to provide a global large-incidence-angle (Sun low to the horizon) basemap and time-lapse movies of the illumination conditions at both poles (Fig. 5). The SCS transfers commands from the spacecraft to the camera to acquire image data, and receives and compresses data en route from the cameras to the spacecraft's solid state recorder. In this paper, we provide an overview of the LROC investigation, present the results of the preflight instrument calibration, and summarize LROC ground operations.

2 LROC Overview and Scientific Objectives

LRO was launched 18 June 2009 on an Atlas V 401 rocket from the Cape Canaveral Air Force Station Launch Complex 41. Following a four day Earth-Moon transit, the spacecraft will enter a 2-month commissioning phase, followed by a year-long nominal mission in a 50×50-km polar mapping orbit. Following the conclusion of the nominal mission, a multi-year extended mission in a fixed 27×216-km orbit is possible.

LROC has been specifically designed to address two of the primary LRO measurement requirements (NASA 2004b).

(1) Assessment of meter and smaller-scale features in order to facilitate safety analysis for potential lunar landing sites near polar resources and elsewhere on the Moon.

One of the two prime objectives of the LROC investigation is to provide the data necessary and sufficient to characterize potential landing sites. The LRO requirement is to

assess the threat posed by "meter and smaller-scale features" (NASA 2004b). This assessment requires a 0.5-m pixel scale in order to ensure unambiguous two-pixel detection of meter-scale features. The NACs will detect blocks down to ~1 m horizontal scale with ≤ 0.5 m heights, and craters with diameters ≥ 2.5 m. In addition to high-resolution imaging, topographic data derived from both geometric and photometric stereo (photoclinometry) observations of potential landing sites at spatial scales of 2 to 5 m/pixel will provide quantitative information about the slopes in small craters that pose a risk for landing spacecraft. From both the Apollo and Surveyor experience, it is known that small craters, rather than blocks, may actually present a greater danger to landing vehicles because they are far more abundant. In fact, except for very young Copernican units, the lunar surface is saturated with craters smaller than 100 m in diameter (Gault 1970). Thus, a lunar landing site will contain many craters, presenting a sub-horizontal surface at the scale of any lander. Blocks, on the other hand, are much less common, especially in areas away from fresh craters (Cameron and Coyle 1971; Cintala et al. 1982; Cintala and McBride 1995; Lee et al. 1986; Moore 1971). The presence of small, shallow craters can be assessed from images with large (> 70°) incidence angles and meter-scale topography. LROC will provide essential morphology information and stereogrammetric and photometric stereo observations for high-priority exploration sites (NASA 2005; Taylor and Spudis 1990).

(2) Acquire multi-temporal synoptic 100 m/pixel imaging of the poles during every orbit to unambiguously identify regions of permanent shadow and permanent or near-permanent illumination.

The Moon's equator is tilted only 1.54° to the ecliptic, so seasonal lighting conditions change only a small amount during a year. Thus there are regions of permanent shadow and permanent or nearly permanent illumination in the vicinity of the lunar poles. Theory as well as radar and neutron measurements suggest that deposits of water-ice (a potentially valuable lunar resource) may occur in permanently shadowed regions near the poles (Feldman et al. 2000; Ingersoll et al. 1992; Nozette et al. 2001; Watson et al. 1961). Regions that are illuminated for extended periods are prime candidates for future lunar bases owing to relatively benign thermal conditions and constant solar power (Goddard 1920; Heiken et al. 1991). Clementine imaged the poles every 10 hours (250 to 500 m/pixel) allowing a synoptic reconstruction of lighting conditions over a period of two Earth months (i.e., two lunar days). At the time of the Clementine mission, the Moon was in southern winter (sub-solar point 1.5°N to 0.3°N), therefore the derived lighting maps more accurately show permanent shadows and near-permanent illumination in the northern and southern hemispheres, respectively. Clementine lighting maps revealed peaks near the South Pole that receive sunlight for almost 70% of a lunar day (Bussey et al. 1999; Noda et al. 2008). Unfortunately, the Moon was in a nearly identical configuration during the Apollo-era Lunar Orbiter polar missions, and so it is not possible to construct maps of regions of anomalously long illumination near the North Pole from any existing data.

In monochrome mode from the nominal 50-km orbit, the WAC FOV covers a swath ~104-km wide resulting in repeat coverage every orbit for the region between 88° and 90° at each pole. LROC will image 80° to 90° on the dayside and back to 80° on the night side on each orbit, enabling the creation of a year-long illumination movie with time steps at least every five hours from ±88–90°, and coverage to 85° with lesser but still sufficient time resolution over a full lunar year. WAC images will provide a calibrated, archived, and reduced dataset completely delimiting permanently shadowed regions and permanently (or near-permanently) illuminated terrain at both poles at a scale of 100 m.

In addition to these two primary objectives, LROC will return six other high-value datasets valuable both for planning future human exploration and supporting basic lunar science investigations.

(3) Meter-scale mapping of regions of permanent or near-permanent illumination of polar massifs.

While the combined NAC FOV will limit its temporal sampling of polar illumination conditions, it can provide meter-scale sampling of the boundaries of shadowed regions and complete mapping of illuminated terrain within 5° of the poles. During respective summers, when shadows are at a minimum, the NAC will acquire hundreds of images at 1-m/pixel to enable mosaics of each pole. The mosaics are built up by first imaging from 87.5° latitude to 0.8° past the pole on one orbit. For the next two orbits, the NACs then image from 85.5° to 88.8°. This three orbit cycle is repeated for 29 days until complete coverage of the map region is obtained. The summer mosaics will serve as a basemap of illuminated regions and will provide high-resolution details of the margins of permanently shadowed regions. During winter much of the polar regions are in shadow, so NAC imaging will concentrate on targets known to have extended periods of illumination. Two massifs near the South Pole collectively receive illumination for more than 95% of a winter day at a scale of ∼200 m/pixel (Bussey et al. 1999; Noda et al. 2008). Lighting conditions of these topographic peaks will be examined at 1 m/pixel over extended periods.

Identification and high-resolution mapping of highly illuminated sites is of critical importance for future human surface operations in the lunar polar region for both power and environmental reasons (Goddard 1920; Heiken et al. 1991; Watson et al. 1961). Since the persistently illuminated regions are by definition massifs, it is probable that their summit areas will receive the most illumination. Such regions could be as small as a few to tens of meters across, below the resolution of other lunar datasets. A 10×10 m region represents 1% of a WAC pixel, 4% of a SMART-1 AMIE pixel, 1 Kaguya terrain camera pixel, and 2×2 Chandrayaan Terrain camera pixels, but will be covered by 400 NAC pixels (20×20). The value of such small areas may actually be very high, providing mission planners with specific areas where installed solar arrays would provide continuous or nearly continuous power to nearby assets. High-priority landing and operational sites will be imaged at full resolution (0.5 m/pixel) allowing characterization of the suitability for landing and surface operations at these high value targets.

(4) Repeat observations of portions of potential landing sites and elsewhere for the derivation of high-resolution topography through stereogrammetric and photometric stereo analyses.

LROC will provide photogrammetric and photometric stereo data for high-priority candidate landing sites and select areas of high scientific interest. Most of the processing for topographic maps will need to be funded by programs other than LRO, but the LROC team will generate example geometric and photometric stereo-based products for select sites to demonstrate the utility of the methods and data reduction procedures. For photometric stereo, at least three nadir observations of the same scene, each under different illumination conditions will be acquired. For geometric stereo, the LRO will have to be rolled into an off-nadir geometry to collect cross-track images at appropriate lighting conditions, but these opportunities will be limited to at most three per 24-hour period due to constraints imposed by other LRO instruments.

(5) Global multispectral observations in seven wavelengths to characterize lunar resources, in particular ilmenite.

The WAC multispectral dataset will allow the science community to improve maps of some mineralogical components of the lunar crust, in conjunction with complementary datasets (Clementine, Kaguya, Chandrayaan-1, and SMART-1). The bandpasses of LROC WAC are particularly suited for the detection of ilmenite ($FeTiO_3$), which is identified as a valuable lunar resource. Ilmenite is notable for being an excellent source of oxygen, titanium metal (Williams et al. 1979; Zhao and Shadman 1993), and solar-wind-implanted volatiles (such as H and He), which are preferentially retained by ilmenite-rich soils (Cameron 1993). Volatile elements may be useful to facilitate the production of water and possibly fuels (H and ^{3}He). The accurate determination of titanium abundance in lunar surface deposits is therefore an import part of lunar resource assessment and development. No funding is provided to construct the global multi-spectral map.

(6) A global 100-m/pixel basemap with incidence angles (60°–80°) favorable for morphological interpretations.

Global coverage at scales of 100-m/pixel and large incidence angles (> 50°) is crucial for systematic geologic mapping and crater counting efforts. High precision crater counts of the lunar surface are especially important because the Moon is the only planetary body for which relative ages from crater counts can be correlated with absolute dating of rock samples collected by trained field observers (Stoffler et al. 2006, and references therein). The best existing lunar morphologic basemap is the recently completed Lunar Orbiter digital mosaic (Becker et al. 2004) with scales ranging from 60 to 600 m/pixel, although this dataset could eventually be superseded by the data collected by instruments aboard recent lunar missions (i.e., Chang'E, Kaguya). The current lack of globally uniform, high-resolution lunar imaging means that large parts of the Moon's surface (especially on the lunar farside) have not been systematically dated using crater statistics. Clementine observations were intentionally acquired at high Sun angles to enhance the analysis of the color data and are not suitable for morphologic mapping at non-polar latitudes (Nozette et al. 1994). LROC WAC will provide imaging to construct a 100-m/pixel global map with incidence angles between 55°–75° (except at in polar regions, where incidence angles are always higher) to enable the creation of a uniform global crater chronology dataset with consistent incidence angles.

(7) Sub-meter imaging of a variety of geologic units to characterize their physical properties, the variability of the regolith, and other key science questions.

The physical properties of the lunar regolith have been characterized in great detail from data and samples returned by Surveyor, Apollo, and Soviet missions. Meteorite bombardment over time has converted crystalline rock to a soil that is essentially uniform in terms of thickness, particle size distribution, bearing strength, cohesion, and many other physical properties (Carrier et al. 1991). This layer is known as the *regolith*, and it covers the entire lunar surface. Regolith typically varies in thickness between 1 and 10 m in the maria, and most likely greater than 10 m in depth in highlands regions (Cintala et al. 1982). All lunar surface operations will take place on or within the regolith, and all exploitable resources and construction materials will come from the regolith, which means that understanding the properties of the regolith is vital for successful lunar surface activities. Although much is known about the physical properties of lunar soils, LROC NAC imaging will provide the necessary data (0.5 m/pixel imaging) needed to apply proven techniques to estimate regolith thickness and other key parameters (Oberbeck and Quaide 1968, 1967; Quaide and

Oberbeck 1968). Among the science questions that will be addressed using LROC NAC images include the rates of regolith generation, local variability in regolith thickness, and the presence within the regolith of coherent blocks.

(8) Meter-scale coverage overlapping with Apollo-era panoramic images (1–2 m/pixel) to document the number of small impacts since 1971–1972. The current impact rate for bolides in the 0.5 to 10 m diameter range is not known to better than 1 or 2 orders of magnitude (Ivanov 2006). Elucidating the impact rate at these sizes enables engineering remediation measures for future surface operations and interplanetary travel.

Particles with masses 50 g to 1000 g (4 to 10 cm diameter at 2 g/cm^3) impact the Moon as often as 10 times/day (Duennebier et al. 1976). LROC NAC observations (0.5 m/pixel) of (1) very young mare surfaces and (2) regions photographed using the Apollo 15–17 Panoramic Camera will be used to place estimates on the number of small craters (1 to 100 m diameter) that have formed from 1971–2010. LROC NAC images will be collected from and compared to as many of the regions with comparable Apollo panoramic camera imaging (i.e., 1 m/pixel) as possible (Lawrence et al. 2008a). This comparison will provide the first direct measure of the current formation rate of 1 to 100 m craters and place an important constraint on the most energetic hypervelocity impact from which future lunar structures must be protected.

3 Instrument Design

Leveraging the extensive experience of LROC prime contractor Malin Space Science Systems (MSSS), the LROC instrument subsystems share heritage from the Mars Color Imager (MARCI) and Context Camera (CTX) aboard the Mars Reconnaissance Orbiter (MRO), the Mars Climate Orbiter (MCO), Mars Polar Lander (MPL), Mars Odyssey, and the Mars Phoenix Lander spacecraft (Malin et al. 2001, 2007; Bell et al. 2009).

3.1 Narrow Angle Cameras (NACs)

The two NACs (Fig. 2), designated NAC-Left (NAC-L) and NAC-Right (NAC-R), are designed to provide 0.5 m scale panchromatic images over a combined 5-km swath. Each NAC utilizes a 700-mm focal-length telescope that images onto a 5000-pixel charge coupled device (CCD) line-array, providing an IFOV of 10 µradians and a cross-track field-of-view of 2.85° each, which yields a total ground track swath-width for both cameras of 5-km at the nominal 50-km altitude. Each NAC internal buffer holds 256 MB of uncompressed data, enough for a full-swath image 25-km in length or a 2× binned image 104-km long. The NAC data are sampled to 12-bits, then companded (bit compression) to 8-bits. Prior to downlink an additional lossless first-difference Huffman compression is applied.

3.1.1 NAC Optics

The principal challenges of the NAC optical design were to provide near diffraction-limited performance at a half-meter ground sample distance over a relatively wide field, in the lunar orbit thermal environment and with low mass. While the starting point for the NAC design was the MRO CTX (Malin et al. 2007), that design was unable to meet these NAC requirements. The NAC resolution requirement was twice that of CTX (10 microradians per pixel rather than CTX's 20 microradians) but with the same field of view. The temperature

range the instrument experiences in lunar orbit is considerably greater than what CTX sees at Mars, prompting us to seek a less thermally sensitive design than the CTX Maksutov telescope. Finally, cost minimization drove the need to maximize the reuse the CTX detector and electronics. Central to our strategy for addressing these requirements was to build two duplicate NACs with offset pointing to provide twice the field of view of a single copy of the instrument.

Using two instances of the instrument to get the full 5.7° swath requires an individual unit FOV of 2.85°. To limit the thermal sensitivity of NAC optics, we pursued optical designs without a large refractive front corrector group. The flight NAC telescope uses hyperbolic primary and secondary mirrors (Ritchey-Chretien, hereafter RC) with an all spherical triplet field corrector lens to provide an optical field of view of approximately 3° (large for an RC design). This f/3.59 telescope had a design MTF at Nyquist of greater than 56% over the entire field. The design also incorporates a 650 mm long sunshade to prevent illumination of the primary mirror by rays more than 30° off axis. The specifications of each of the two NAC telescopes are given in Table 2. To minimize both mass and thermal sensitivity, the metering structure is made of graphite-cyanate composite. Because of the composite resin is hygroscopic, there is a significant focus shift between fully dry, the case which pertains to lunar orbit, and "wet," the state the instruments were in the laboratory environment. Validation of focus for flight was by baking-out the cameras in at 65°C in vacuum while imaging a collimator stimulus. A final confirmation of focus was made by imaging the Moon immediately after removing each unit from thermal vac (Fig. 21). The NAC telescopes were built by Light-Works Optics of Tustin, CA in collaboration with Vanguard Composites of San Diego, CA.

3.1.2 NAC Electronics

The NAC electronics design is based on the Context Camera (CTX) on the Mars Reconnaissance Orbiter (MRO) mission, with modifications to increase the maximum pixel rate from 2 megapixels/second to 7.5 megapixels/second. The electronics are built around the Kodak KLI-5001G line array. This device is a 5064-element CCD with 7 micron pixels, and an average QE through the instrument bandpass of $>60\%$. It is fabricated in an NMOS two-metal two-poly process by Kodak Image Sensor Solutions in Rochester, NY. Correlated Double Sampling (CDS) is incorporated on-chip. The device has dual readouts with a maximum readout rate of 12.5 MHz. Though the datasheet noise floor is fairly high (150 e^- at room temperature and 12.5 MHz operation) performance is better at operating temperature and slower clocking.

The NAC analog signal processing chain is considerably simplified by the on-chip CDS provided by the CCD. There are two duplicate analog signal chains, one handling the even pixels, the other handling the odd pixels. Although CDS is performed on the CCD die, the output signals still have a large DC pedestal, which varies device-to-device and (potentially) with temperature and radiation exposure. To mitigate excess background the design includes a black-level DAC that allows a constant black level to be removed prior to amplification. The black level was established during calibration and can be changed via ground command. The digitization range is set to 300 Ke^- maximum, yielding a scale factor of about 90 e^-/DN (90.5 NAC-L and 92.5 NAC-R), which is close to the best-expected noise performance of the CCD.

The NAC digital electronics provides clock generation, sampling of the CCD signal, conversion of the 12-bit samples to 8-bit encoded pixels, storage of the pixels, and finally readout of the pixels to the SCS. A dedicated field-programmable gate array (FPGA) rather than a general-purpose processor performs these functions. The specific functions implemented in the FPGA are:

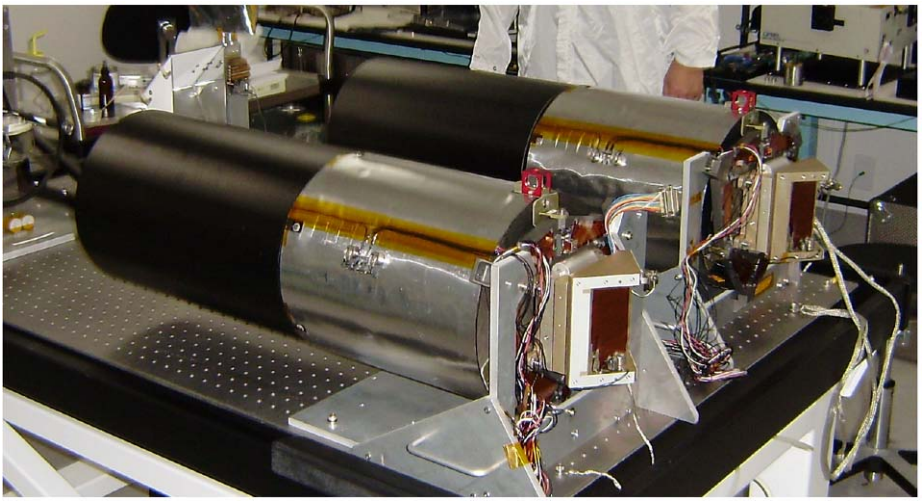

Fig. 2 The LROC Narrow Angle Cameras side by side without their radiators. The black baffle prevents stray light from entering the optics (silver part of the tube). The focal plane array and associated electronics are in the triangular housing on the right end. The diameter of each tube is 27 cm

- Serial command interface from the SCS
- Serial data interface to the SCS
- DRAM interface
- CCD clock generation
- 12-to-8 bit pixel companding
- Commanding and DRAM readout

The NACs use 256 Mbit synchronous DRAM for image storage. Eight devices provide a total capacity of 256 MB (268,435,456 bytes). Each pixel value is mapped through an adjustable piecewise linear transfer function. Approximate square root encoding allows conversion of 12-bit per pixel data to 8-bit form with only minimal loss of information. Since the transfer function can be changed in flight, other forms of encoding (e.g., linear with offset) can be used as well (see Appendix A).

The SCS communicates with the NAC via a 3-signal (data, clock, and enable) synchronous serial LVDS interface, at a maximum clocking rate of 2 MHz. The command interface section of the FPGA is clocked by the interface clock and its outputs are synchronized to the system clock domain using dual flip-flops. The instrument communicates with the SCS via a 3-signal (data, clock, and enable) synchronous serial interface, at a maximum clocking rate of 30 MHz.

Only minimal instrument health monitoring is provided in the form of a thermistor at the focal plane (backside of CCD), at the field programmable gate array (FPGA) in the electronics box, and on the metering structure between the primary and secondary mirrors. Operating temperatures of the focal plane are expected to range from 0°C to 20°C over the course of the mission, mostly a function of local time-of-day.

3.1.3 NAC Orientation

The NACs are mounted on the spacecraft such that the CCDs are perpendicular to the spacecraft's X-axis. The NAC-L is off-pointed ∼2.85° from the NAC-R so that the footprints of

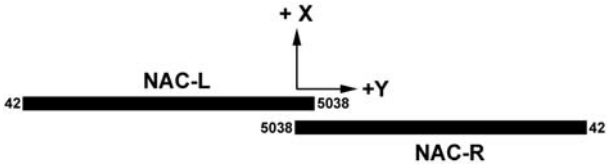

Fig. 3 Orientations of NAC CCDs as mounted on the spacecraft. Numbers show pixel addresses (zero based coordinates). The NACs overlap ∼135 pixels in the crosstrack direction (Y) and are separated ∼0.106° (185 pixels) downtrack (X)

the two images overlap only ∼135 pixels. The NAC-R is also mounted 0.106° forward of the NAC-L. The NACS are mounted such that pixel 0 for the NAC-L is at the −Y (in spacecraft coordinates) end of its CCD and pixel 0 for the NAC-R is at the +Y end of its CCD (Fig. 3). This orientation requires that one of the NAC frames from a NAC-L and NAC-R paired observation must be transformed such that both images have the same ground orientation.

3.2 Wide Angle Camera (WAC)

The WAC (Fig. 4) is designed to provide global imaging at a scale of 100 m/pixel in seven color bands over a 105-km swath in monochrome mode and 57-km in color mode. The LROC WAC uses a 1000 by 1000 pixel CCD that has seven narrow-band interference filters bonded to the detector. Two of the filters are in the ultraviolet (UV) and five are in the visible. The WAC has two short-focal-length lenses, one UV and one visible, both of which image onto the same detector. From the nominal 50-km altitude orbit in monochrome imaging mode, the WAC will provide a nadir ground sample distance of 75 m/pixel (98 m/pixel at far field). In the UV system, the nadir resolution is 384 m/pixel. The seven-band color filter array provides different sections of the CCD with different bandpasses. Repeated imaging at a rate such that each of the narrow framelets of each color band overlap provides continuous coverage in any one color ("push-frame imaging"). The layout of the WAC filters is similar to the MRO MARCI instrument as described in Bell et al. (2009). WAC pixel values are digitized to 11-bits and subsequently companded to 8-bit values. After transmission to the SCS, the WAC data have a lossless first-difference Huffman compression that is applied prior to downlink.

3.2.1 WAC Optics

The WAC optics consist of four optical elements: the visible lens, the UV lens, the prism and the color filter array (CFA). The visible lens has a 6.0 mm focal length and a focal ratio of 5.5. It has six fused silica elements and is optimized for the wavelength range from 395 nm to 690 nm. It provides a 90° field of view over the full 1008 pixel width of the detector. The lens has a design MTF of greater than 60% at 56 line pairs per mm in all bands. The UV lens has a 4.7 mm focal length and a focal ratio of 5.1. It has five elements and is optimized for the wavelength range from 290 nm to 370 nm. It provides a 60° field of view over a 512 pixel width on the detector. Because signal is low in the UV bands, the UV system data is acquired by summing pixels 4 × 4. The optical design provides a 4 by 4-pixel ensquared energy of greater than 80% in both UV bands. The physical diameter of each of these lenses is greater than the format of the CCD detector. A prism is used to allow both lenses to image on the same CCD. This prism provides a straight-through path from the visible lens to the detector, and a periscope-type optical path for the UV lens. The latter

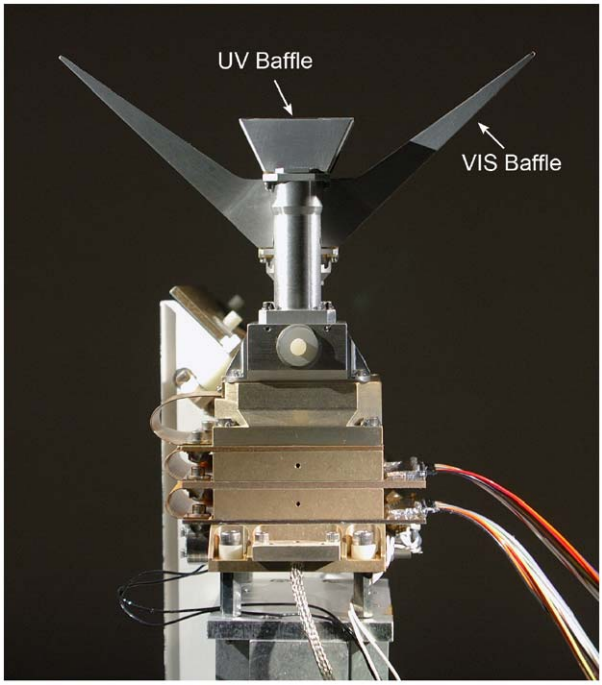

Fig. 4 LROC Wide Angle Camera. The width of the visible optic baffle is 15.95 m (Image credit: Mike Malin, Malin Space Science Systems, Inc.)

offsets the point at the UV image is formed laterally, placing it closer to the visible image (and therefore on the photoactive area of the detector). Each lens and the prism are integrated and aligned into a signal assembly with the WAC detector and electronics. The color filter assembly (CFA) is a 9.5 mm by 9.3 mm by 0.6 mm fused silica substrate with seven vacuum deposited interference filters laid down is the geometry appropriate for push-frame imaging. It is bonded to the surface of the CCD detector with optical cement. The final focusing of the system is done by lapping a spacer between the CCD package and the back of the prism housing. The WAC lens/prism assembly was built by LightWorks Optics and the CFA was manufactured by Barr Associates of Westford, MA.

3.2.2 WAC Electronics

The WAC electronics are designed around the Kodak KAI-1001 Charge-Coupled Device (CCD) detector. This detector has 1024 × 1024 9-µm pixels (1018 × 1008 photoactive, others masked for background/bias signal determination) and uses interline transfer to implement electronic shuttering. The KAI-1001's fill factor of 20% causes its quantum efficiency to be low, but the WAC optics are sufficiently "fast" to compensate and thus provide the required system sensitivity. To support selection of data through specific bands of the color filter array (CFA), the CCD's fast-dump feature can be used to read out only selected portions of the detector.

The output signal from the CCD is AC-coupled and then amplified. The amplified signal is digitized to 12-bits at 3 Mpixels/s. For each pixel, both reset and video levels are digitized and then subtracted in the digital domain to perform correlated double sampling (CDS), resulting in a net 11-bits of dynamic range. The digital electronics are responsible for clock generation, sampling of the CCD signal, conversion of the 11-bit samples to 8-bit

encoded pixels, storage of the pixels, and readout of the pixels to the SCS. These functions are performed by a digital signal processor (DSP) with software emulation.

WAC instrument health monitoring includes real-time telemetry monitoring of voltage and temperature during S-band contacts, and trend analysis of voltage and temperature using stored telemetry downlinked during Ka-band contacts. Additional health monitoring is performed by statistical analysis of acquired images, especially WAC dark pixels.

3.2.3 WAC Monochrome Imaging

The highest-resolution existing morphologic basemap is the Lunar Orbiter digital mosaic (Becker et al. 2004) with resolutions ranging from 60 to 600 m/pixel (Bowker and Hughes 1971). The WAC will accordingly be operated in single-band mode (nominally the 605 nm filter) to acquire a global morphology basemap with incidence angles between 60° and 80° to provide an improved morphologic map of the Moon at a uniform resolution of 100 m/pixel.

3.2.4 WAC Multispectral Imaging

The WAC has two ultraviolet filters (320 and 360 nm), and five visible filters (415, 565, 605, 645, and 690 nm). These bandpass filters were selected to characterize spectral features for some common minerals found at the lunar surface and will complement Clementine UVVIS (415, 750, 900, 950, 1000 nm) and NIR datasets (1100, 1250, 1500, 2000, 2600, 2780 nm) (Nozette et al. 1994) as well as VIS-NIR data being collected by Chandrayaan-1 and Selene (Haruyama et al. 2008; Green et al. 2007).

The UV bandpasses are sensitive to the distribution of some opaque minerals such as ilmenite, which have a distinctive UV spectral signature consisting of a characteristic absorption between 450 and 500 nm (Fig. 5). This band results in a flat to upturned signal in the near-UV relative to other common lunar minerals (Wagner et al. 1987). The WAC visible bandpasses are also sensitive to large variations in the magnesium to iron ratio (magnesium number) of olivine, which exhibits maxima at 550 nm to 700 nm as the iron content increases (Fig. 6).

3.3 Sequence and Compressor System

The Sequence and Compressor System (SCS) interfaces the WAC and two NACs to the spacecraft avionics (Fig. 7). The SpaceWire link between the SCS and the spacecraft oper-

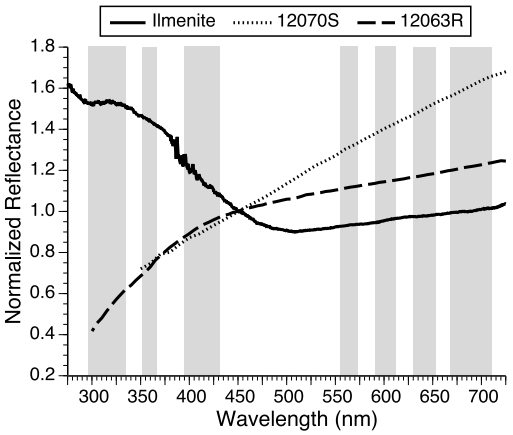

Fig. 5 Spectra of ilmenite (*solid line*) showing a broad minima at 500 nm. The WAC has the unique ability to acquire measurements in the UV (bandpasses at 320, 360 nm) that are well suited to discriminate ilmenite from other common lunar minerals. Low titanium rock (*dashed line* 12063R) and soil samples (*dotted line* 12070S) are plotted for reference (normalized at 450 nm). FWHM of the WAC bandpasses are shown as *gray bars*

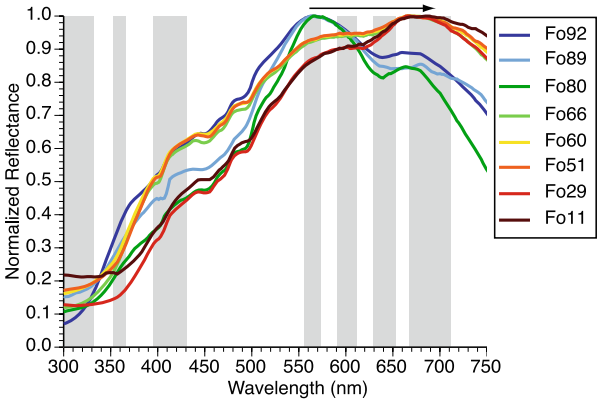

Fig. 6 Spectra of olivine as a function of Fo-number (i.e., Mg relative to Fe content). The *arrow* indicates the migration of the reflectance peak to longer wavelengths as the Fo number decreases. Spectra from RELAB public database, Brown University. LROC WAC bandpasses are shown for reference

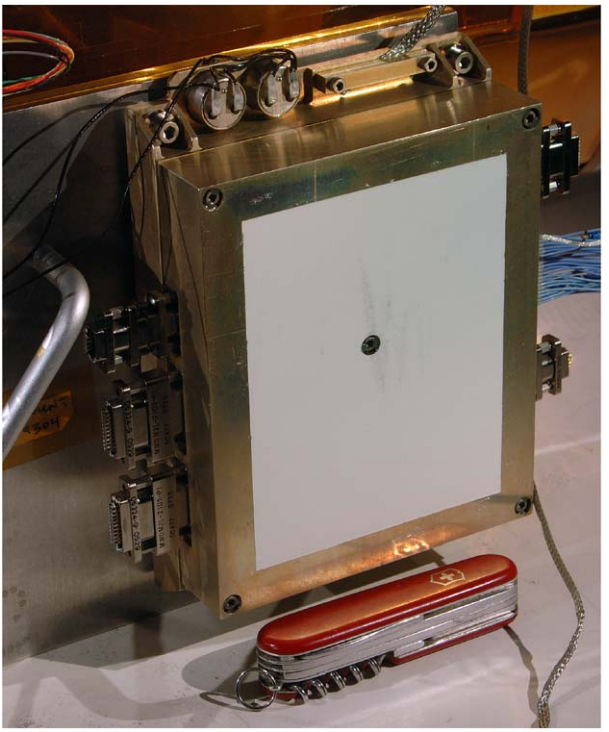

Fig. 7 LROC Sequence and Compressor System (Image credit: Mike Malin, Malin Space Science Systems, Inc.)

ates at 2 Mbit/s while transferring commands to the SCS, and 40 Mbit/s carrying telemetry from the SCS to the spacecraft. Each NAC command/data interface is comprised of two synchronous serial 3-wire LVDS links; one transmits commands from the SCS to the NAC at 2 Mbit/s and the other receives NAC telemetry at 30 Mbit/s. The WAC command/data interface is comprised of a synchronous serial 4-wire RS-422 link that operates at 2.5 Mbit/s with a data signal in each direction and a common clock and frame signal generated by the SCS.

The SCS, WAC and NACs are powered directly from the spacecraft 28 V power bus, on separately switched circuits. The WAC heritage design includes an internal power switch and

requires its DSP firmware to be loaded from an external source immediately after application of power. Both of these functions are provided by the SCS.

The core functionality of the SCS is implemented in a Xilinx Virtex-II FPGA. All interface, compression, and timing functions are implemented as logic peripherals to a MicroBlaze soft-processor core in that FPGA. NAC telemetry streams through the SCS in real-time, with minimal FIFO buffering and optional Huffman predictive compression performed in logic. To accommodate the interleaving of WAC and NAC data onto the single spacecraft interface, the SCS includes a double-buffer for WAC image frames. WAC data may also be compressed with a dedicated Huffman Compressor.

4 Instrument Calibration

The exploration and science goals of the LROC investigation require an accurate preflight calibration of the instrument system (i.e. optics, filters, detectors, and electronics), as well as continuing calibration activities in flight to ensure stability over the course of the mission. To those ends, the LROC team executed a comprehensive ground calibration sequence designed to accurately measure the response of the WAC and the NAC instruments to known, calibrated inputs. This section details the LROC instrument calibration results. The properties of the LROC cameras are summarized in Tables 2 and 3.

System-level testing of the LROC instruments was conducted using the facilities and equipment at MSSS (ambient laboratory calibrations), the University of California in San Diego (instrument thermal-vacuum tests) and the NASA Goddard Space Flight Center (LRO spacecraft thermal-vacuum tests). The calibration tests are listed in Table 1. Since the NAC design is based on the MRO/CTX camera and the WAC design on the MRO/MARCI camera, with the CCD detectors and electronics of the same type, the CTX/MARCI characterization tests described in Malin et al. (2005) and Bell et al. (2009) are both useful references.

Table 1 Calibration tests conducted for both NACs and the WAC. For the WAC, the test was done for each filter, if applicable

Calibration test	Description
Dark imaging	Determine dark current and bias; optimization of NAC bias level (DAC offset setting)
CCD performance validation and linearity	Measure linearity and photon transfer curve (gain, read noise, full-well)
Flat-field imaging	Measure system response non-uniformity on a pixel-by-pixel basis
System spectral response	Determine relative system throughput (in-band) and characterize out-of-band leaks
Absolute and relative radiometry	Determine conversion between measured DN and radiance units
Geometric calibration	Determine focal length, field of view and geometric distortion
Focus tests	Determine focus and MTF by imaging a bar target
Stray light test	Determine light scattering from out-of-field sources

Table 2 NAC system performance (where only one value is given it applies to both NACs)

Parameter	Performance NAC-L	Performance NAC-R
FOV	2.8502°	2.8412°
IFOV (nadir)	10.0042 µrad	9.9764 µrad
image scale at 50-km altitude	0.5 meter/pixel	
max. swath size at 50-km altitude	2.49 × 26.1-km	2.48 × 26.1-km
f/#	3.577	3.590
focal length	699.62 ± 0.08 mm	701.57 ± 0.09 mm
distortion coefficient k	0.0000181 ± 0.0000005	0.0000183 ± 0.0000005
optical center location	sample 2548 ± 8	sample 2568 ± 8
primary mirror diameter	198 mm	
system MTF (Nyquist)	0.23	
Gain	90.5 ± 2.6 e^-/DN	92.5 ± 1.5 e^-/DN
detector noise	101 ± 7 e^-	97 ± 1 e^-
detector full-well	334,000 ± 31,000 e^-	352,000 ± 4100 e^-
SNR (mare at 70° incidence angle)	> 42	> 42
Spectral response	400–760 nm	
radiometric accuracy*	1% relative, 10% absolute	
detector digitization	12 bit, encoded to 8 bit	
data link to SCS	LVDS, 30 Mbps	
temperature sensors	2 per electronics box, 2 per telescope	
lossless compression ratio	1.7:1	
Voltage	28 ± 7 V DC	
peak power	9.3 W	
orbit average power	6.4 W	
mass (both NACs)	16.4 kg	
volume (length x diameter)	118 cm × 27 cm (incl. radiator)	

*requires in-flight verification

4.1 NAC Calibration

4.1.1 Detector Characterization

The NAC utilizes a Kodak KLI-5001G linear array CCD that is read out with dual shift registers; channel A for the even pixels, and channel B for the odd pixels. The first 39 pixels are masked for dark signal monitoring, followed by 4 transition (non-imaging) pixels, then 4996 imaging pixels, then 4 transition pixels followed by 21 masked pixels.

The gain, read noise, and full-well of the NAC sensors were determined using the photon transfer method described in Janesick (2007). The setup for this experiment was a Quartz-Tungsten-Halogen (QTH) lamp illuminating a Spectralon® panel. At a given current setting, several images covering all exposure times between 0.34 ms (shortest possible) and 35.25 ms (longest possible) were acquired. After dark signal subtraction, the read-plus-shot noise and the shot noise were plotted versus the signal (the total noise also includes the fixed-pattern-noise). A NAC-L photon transfer curve is presented in Fig. 8, with the resulting derived parameters listed in Table 2. Precision was estimated by varying the endpoints of the linear

Table 3 WAC system performance

Parameter	Visible	UV
FOV (monochrome/color)	91.9°/61.4°	59.0°
IFOV (nadir)	1.498 mrad	7.672 mrad (4 × 4 binning)
image scale (nadir, 50-km altitude)	74.9 m/pixel	383.5 m/pixel
image frame width monochrome	104.6-km	–
image frame width 7-band color	59.6-km	56.8-km
image format monochrome	1024 samples × 14 lines	–
image format color (for each band)	704 samples × 14 lines	128 samples × 4 lines (binned)
f/#	5.052	5.65
focal length	6.013 mm	4.693 mm
system MTF (Nyquist)	0.37	
Gain	25.9 ± 0.7 e^-/DN	
detector noise	66 ± 4 e^-	
detector full-well	$46{,}100 \pm 3600$ e^-	
SNR (at 1000 DN)	> 150	
radiometric accuracy*	1% relative, 10% absolute	
detector digitization	11 bit, encoded to 8 bit	
data link to SCS	RS422, 2.5 Mbps	
temperature sensors	1	
lossless compression ratio	1.7:1	
Voltage	28 ± 7 V DC	
peak power	2.7 W	
orbit average power	2.6 W	
Mass	0.9 kg	
volume (width × length × height)	15.8 cm × 23.2 cm × 32.3 cm (incl. radiator)	

*requires in-flight verification

fit range, the number of pixels used for analysis, and the determination of the read noise. Above 200 DN both NACs have a highly linear response (Fig. 9).

4.1.2 NAC Calibration Pipeline

The image calibration pipeline for the NACs can be expressed with the following equation:

$$I_{cal}(x,\tau,T) = \frac{(I_{raw}(x,\tau,T) - m_I(\tau,T)) - (D(x,\tau,T) - m_D(\tau,T)) - S(x) - L(I_{off},x)}{F(x)\cdot\tau\cdot r},$$

where,

$I_{cal}(x,\tau,T)$ is the calibrated signal value of pixel x at exposure time τ and temperature T in radiance units of $\mu W/(cm^2 \cdot sr \cdot nm)$,
$I_{raw}(x,\tau,T)$ is the pixel's raw signal in DN,
τ the exposure time,
m is the mean DN value of the masked pixels,
$D(x,\tau,T)$ is the library dark image correction array,
$S(x)$ is the non-linearity offset array,

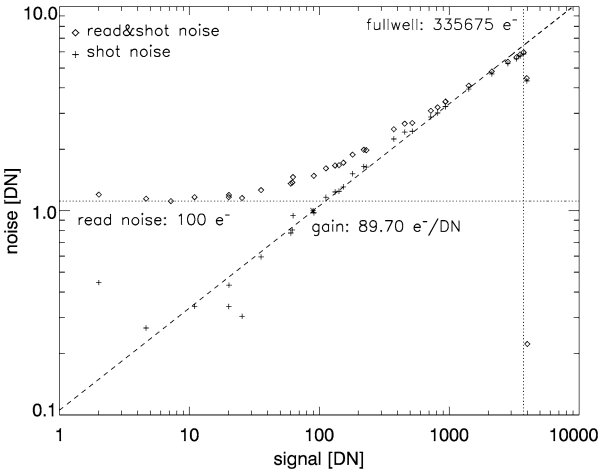

Fig. 8 Photon transfer curve for NAC-L. The linear fit of the shot noise between signal levels of 600 DN and 3000 DN yields a gain of 89.7 e^-/DN. This value is within the uncertainty range of 2.6 e^-/DN (average of 90.5 e^-/DN), which was estimated by varying the endpoints of the linear fit range, the number of pixels used for analysis, and the determination of the read noise

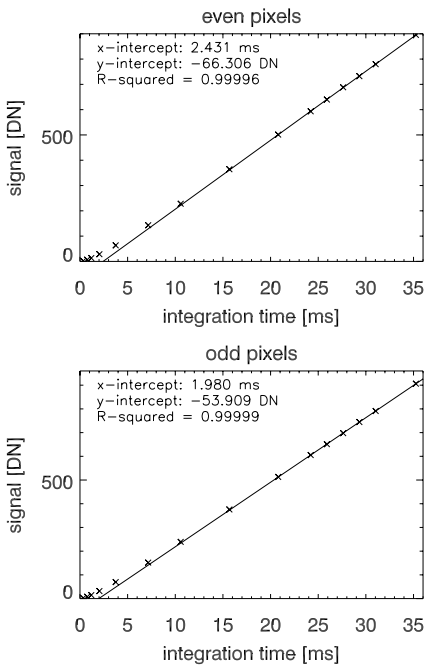

Fig. 9 NAC-R linearity fit for pixel-averaged DN values above 600 DN (dark corrected). Signal response is non-linear for exposure times below 10 ms. The averages of all even illuminated pixels yield a y-intercept of about −66.3 DN (*top*). The corresponding linear fit for the odd pixels yields a y-intercept of −53.9 DN (*bottom*)

$L(I_{off}, x)$, with $I_{off} = I_{raw} - m_I - (D - m_D) - S$, is the logistic function value for low-signal non-linearity correction (only if $I(x, \tau)_{raw} < 600$ DN),

$F(x)$ is the sensitivity non-uniformity array (flat-field), and

r is the spectral responsivity for conversion of DN into radiance units.

The individual steps are discussed in detail in the following sections (Fig. 10).

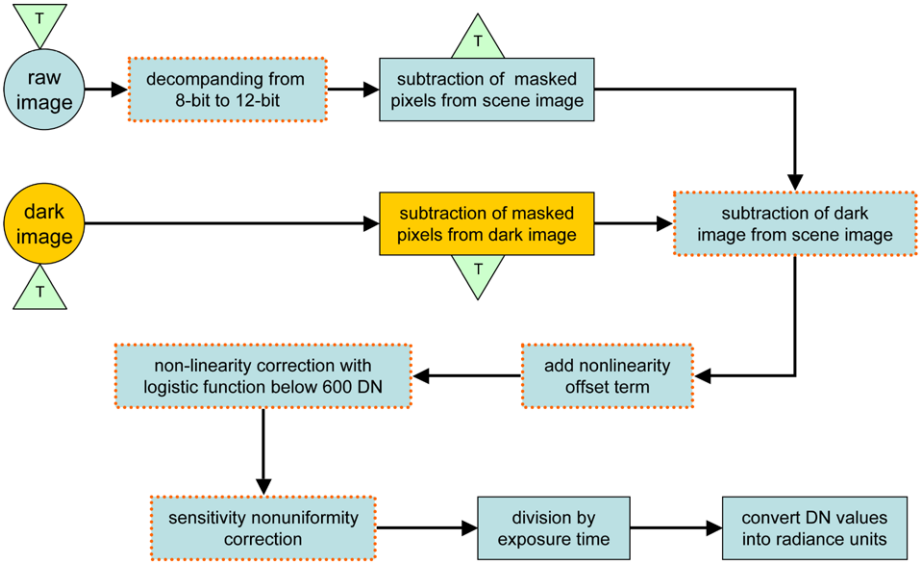

Fig. 10 Schematic overview of the NAC calibration pipeline. Depending on the electronics temperature "*T*," images have a different bias level, which is subtracted with the masked pixels (both for the raw scene image and the library dark image). The library dark image subtraction then corrects the pixel-to-pixel variation of the dark current. The non-linearity correction is a two-step process applied to DNs below 600: additive offset term and a linearization process using a logistic function. The final steps are sensitivity non-uniformity correction (flat-fielding), division by exposure time, and the conversion into radiance units. Steps applied on a pixel-by-pixel basis are indicated with orange dotted border

4.1.3 Interleaving and Conversion to 12 bits

For each NAC the even and odd pixels are read out independently during image acquisition. This strategy enables line readout and transfer to the buffer in the required 337.6 microseconds that corresponds to one pixel of down-track ground motion (nominal 50-km orbit). The even and odd pixels are stored in separate buffers and thus raw data files must be interleaved to form a coherent image. The 12-bit pixel values are companded to 8-bit values using one of six on-board schemes, three schemes are optimized for different signal levels, one is general purpose, while two others are used for calibration sequences (Fig. 11). To enable the fast pixel readout each bit-compression scheme consists of a piecewise linear function composed of up to 5 segments. After ground reception, these 8-bit digital values are converted back to 12-bit with the corresponding decompression tables. The linear functions of each segment are listed for each table in Appendix A.

4.1.4 Bias Level and Dark Images

The offset level of the digital-to-analog converter (DAC) determines the bias level for digitization, i.e. the coarse DN value of a dark image (no incident photons) at shortest exposure. A finer adjustment of the bias level is set with an additional offset parameter for each even and odd channel. Using dark images acquired during thermal vacuum tests, the dependence of the DAC offset setting as a function of focal plane temperature was determined. Thus, in flight, the bias level will be optimized for each individual image based on predicted detector temperature and exposure time (*cf.* Fig. 12).

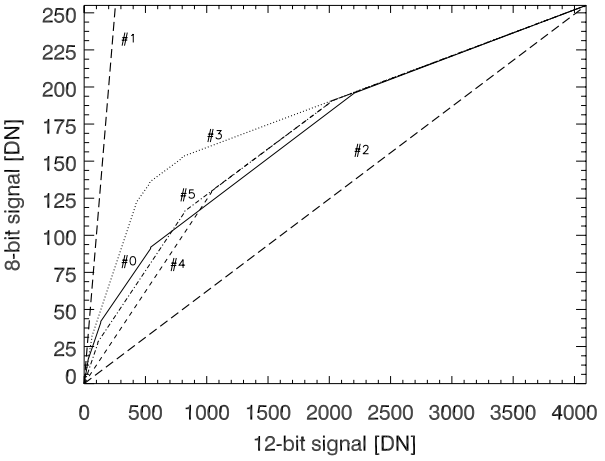

Fig. 11 Six NAC bit-compression schemes (12-bit to 8-bit). Scheme #0 approximates a square root function, scheme #1 is used for dark imaging, scheme #2 bins the input into 16-bit bins, and the remaining are options optimized for different illumination conditions (dim scene, scheme #3; bright scene, scheme #4; cap quantization error, scheme #5)

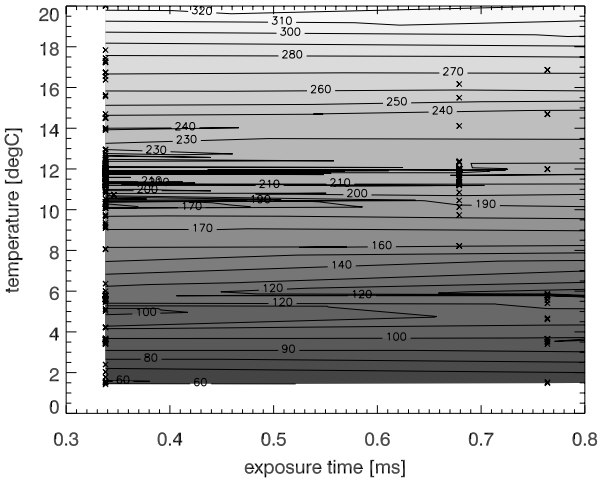

Fig. 12 The dependence of the dark signal (shown as contour lines in DN; for NAC-L even pixels) on exposure time [ms] and temperature [°C]. These data are used to optimize the bias level for each image

In the NAC calibration pipeline (Sect. 4.2.2), the background level, which is the sum of bias and dark current, is removed by subtracting the average of the masked even (odd) pixels on the edges from each illuminated even (odd) pixel. This step is done line-by-line in order to compensate for increase in electronics temperature over a full 52,224-line image that results in an increase of the dark current of up to 3 DN.

Subtraction of the masked pixels corrects the overall average value of the background level, but not pixel-to-pixel variations. This high frequency term is characterized from a library of dark images acquired in thermal vacuum tests over a range of operating temperatures (and eventually with flight data). The average background level is removed from the library dark image in the same manner as the surface image, by subtracting the masked pixel value. After the masked-pixel subtraction the library dark image is averaged over lines and converted into a one-line correction array. Because the background-subtraction is done for both the scene and the library dark image it is not necessary to have a library dark image with the same DAC and offset value. The library dark image subtraction only corrects for the pixel-to-pixel variations of the dark current.

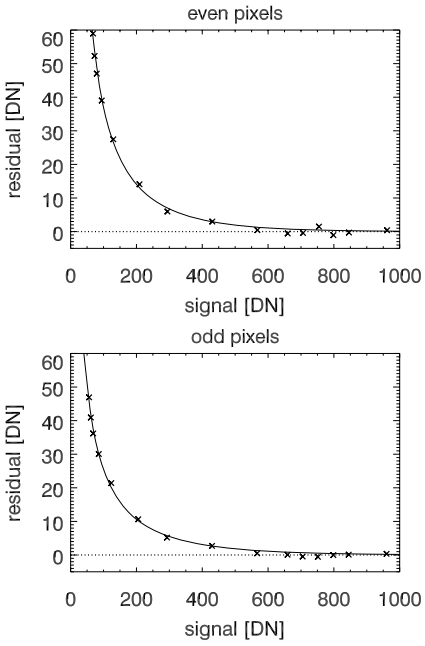

Fig. 13 The residual DN values (measured signal values minus linear fit values) plotted against the offset-corrected signal values follow a logistic function of the form $1/(a \cdot b^x + c)$. Here the results from averaged NAC-R images are shown. The resulting even parameters of the logistic function are $a = 0.03359405$, $b = 1.00561273$ and $c = -0.03180369$ (*top*). The odd parameters are $a = 0.05827176$, $b = 1.00466108$ and $c = -0.05361603$ (*bottom*). If the measured signal is below 600 DN the value calculated from the logistic function is subtracted from the offset-corrected signal in order to linearize the signals

4.1.5 Non-linearity Correction

NAC response at low signal levels (below 600 DN) is non-linear (Fig. 9). The required linearity correction is a two-step process. First a non-linearity offset term is calculated for each pixel (4996 array) as the y-intercept of the linear fit of the background-corrected data between 600 DN and 2000 DN. This offset term is independent of the DAC setting, i.e. the non-linearity depends on the magnitude of the incoming signal.

The second step is performed only for pixel values below 600 DN (background corrected). The difference $L(x)$ between the actual measured signal (after the non-linearity offset correction) and the expected signal from the linear fit function follows a logistic function of the form:

$$L(I_{off}, x) = \frac{1}{a(x) \cdot b(x)^{I_{off}(x)} + c(x)}$$

where $I_{off}(x)$ is the background and non-linearity offset corrected signal in DN (Fig. 13). After applying the non-linearity offset term to all values, those below 600 DN are linearized by simply subtracting the linearity residual $L(x)$ from the input $I_{off}(x)$.

4.1.6 Sensitivity Non-uniformity Correction

Laboratory flat-field images were acquired by evenly illuminating a Spectralon panel with Britek photo studio lamps powered by regular AC current. The setup is basically the same as shown in Fig. 18, just without the black plate. Several thousand integrations were acquired with various exposure times. Small cyclic brightness variations caused by the AC current are eliminated by line averaging. The line-averaged flat-field images are then normalized to the mean value of the central 500 pixels providing a sensitivity non-uniformity correction array. For illustration the non-uniformity arrays of both NACs are presented in Fig. 14.

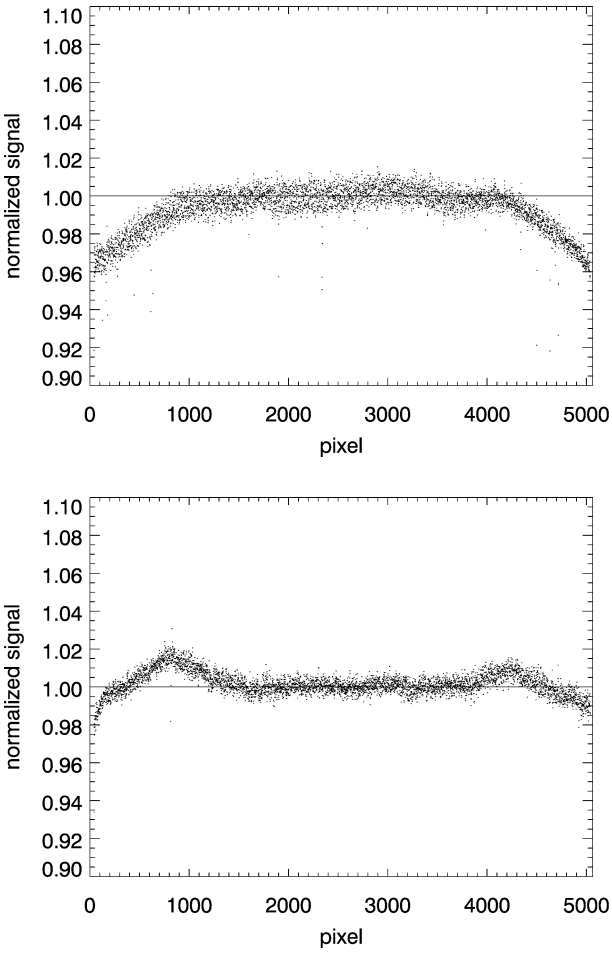

Fig. 14 (*Top*) NAC-L non-uniformity array. (*Bottom*) NAC-R non-uniformity array. Both are the average of 2560 lines and normalized to the mean of the central 500 pixels

4.1.7 Spectroradiometric Calibration

The experimental setup to measure the spectral responsivity $r(\lambda)$ [(DN/s)/(μW/(cm2·sr·nm))] of each NAC consisted of a monochromator with a Xenon lamp. The exit slit of the monochromator was effectively a point source a few meters distant from the NAC. The source was offset in the aperture so that the secondary mirror would not block it. The resulting out of focus image had a spatial FWHM, identical at the different wavelengths, of approximately 2000 pixels. Both the spectral FWHM of the monochromator and the wavelength step-size were set to 10 nm. At each wavelength step the power output of the monochromator was recorded, using an Oriel model 71639 calibrated silicon photodiode fed by a beam-splitter mounted after the exit slit of the monochromator. In addition, before each NAC calibration the monochromator spectral irradiance at the aperture of the NAC was sampled at the brightest spot of the beam by a calibrated spectroradiometer at each wavelength. These power measurements represent only a relative responsivity $r_M(\lambda)$. Absolute calibration was obtained by analyzing flat-field and background corrected images (see Sect. 4.1.6) dividing the image's count rate S [DN/s] by the integral over the relative responsivity multiplied with

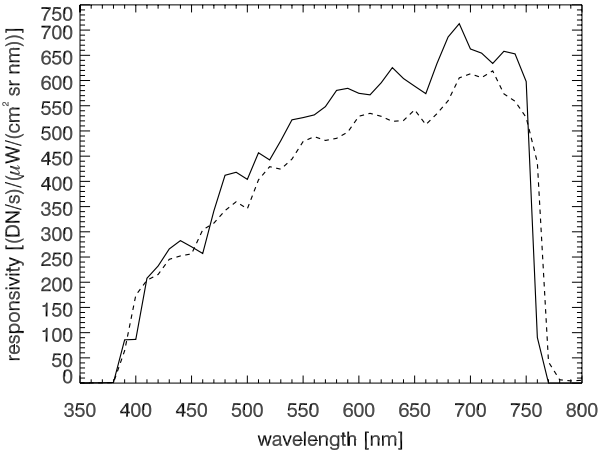

Fig. 15 Spectral responsivity of NAC-L (*solid line*) and NAC-R (*dashed line*). The high-frequency variation reflects noise in the measurement, but have no significant effect on the derived calibration

the spectral radiance of the source $I'_S(\lambda)$ [μW/(cm^2·sr·nm)]. This spectral radiance was measured with a spectroradiometer. However, it turned out that the spectroradiometer measurements had a systematic error that required a cross-calibration with a calibrated integrating sphere in order to obtain the necessary scaling factor $\gamma = 2.3 \pm 0.1$. Thus $I_S(\lambda) = \gamma \cdot I'_S(\lambda)$. In other words, for the absolute calibration the relative responsivity $r_M(\lambda)$ was scaled by a factor equal to the ratio of the actual count rate S observing the laboratory source to the count rate predicted if the absolute responsivity were equal to the relative responsivity. This approach can be expressed as follows:

$$r(\lambda) = r_M(\lambda) \cdot \frac{S}{\int_{\lambda'} r_M(\lambda') \cdot I_S(\lambda') d\lambda'}.$$

The spectral responsivity characterization (Fig. 15) allows the calibrated DN values to be converted to radiance. For a given observation the measured count rate S_L [DN/ms] constitutes the spectral radiance $I_L(\lambda)$ of the lunar scene weighted by the NAC responsivity, i.e.:

$$S_L = \int_{\lambda} r(\lambda) \cdot I_L(\lambda) d\lambda.$$

So the weighted mean radiance measured by the NAC is:

$$\overline{I} = \frac{\int_{\lambda} r(\lambda) \cdot I_L(\lambda) d\lambda}{\int_{\lambda} r(\lambda) d\lambda} = \frac{S_L}{\int_{\lambda} r(\lambda) d\lambda} = \frac{S_L}{r_{NAC}}.$$

The radiometric conversion parameters are $r_{NAC\text{-}L} = 180.56$ (DN/ms)/(μW/(cm^2·sr·nm)) and $r_{NAC\text{-}R} = 166.83$ (DN/ms)/(μW/(cm^2·sr·nm)).

Radiance can be further converted into the reflectivity I/F (Minnaert 1961), with I the observed radiance depending on the observation geometry and F the solar radiance coming from a normally illuminated Lambertian surface. The term I/F is also called radiance factor by Hapke (1993).

With Φ_E the solar irradiance at a distance of 1 AU the measured reflectivity of a lunar scene is:

$$I/F = \frac{I_L \cdot \pi \cdot d^2}{\Phi_E}$$

with d [AU] the distance Sun–Moon. With the formulas above the weighted mean of I/F as measured by the NAC is:

$$\overline{I/F} = \frac{\int_\lambda r \cdot I/F \cdot \Phi_E d\lambda}{\int_\lambda r \cdot \Phi_E d\lambda} = \frac{S_L \cdot \pi \cdot d^2}{\int_\lambda r \cdot \Phi_E d\lambda} = \frac{S_L \cdot d^2}{\varphi_{NAC}}.$$

Using the solar irradiance Φ_E at 1 AU of (Allen 1976) the conversion parameters are $\varphi_{NAC\text{-}L} = 9308.5$ (DN/ms)/AU^2 and $\varphi_{NAC\text{-}R} = 8504.1$ (DN/ms)/AU^2.

Finally, the signal-to-noise ratio (SNR) is calculated from assumed radiances for mare and highlands materials under various incidence angles. The signal is the expected mean radiance for those conditions, and the noise is composed of read noise, shot noise and quantization noise. The minimum SNR is estimated with a 70° solar incidence angle on mare material and presented in Table 2.

4.1.8 Geometric Calibration

Geometric calibration was performed for both NACs by rotating each instrument on a high-precision Ultradex rotary stage and imaging a bar pattern. In this experiment the bar pattern is at the focus of a collimator of identical optical design to the NAC. The bar target is tilted with respect to the collimator focal plane, so the bars are in focus only at one place in the image and progressively go out of focus toward the edges of the image. The Ultradex stage rotations are only in steps of one degree, accurate to better than one arc second, and thus direct collection of sample versus angle can provide only three data points across the detector. Because distortion of over ten pixels is expected for these optics, finer sampling is required. Thus the basic data set obtained was a series of measures of the number of samples that subtend one degree at different locations across the detector. These observed values can then be compared to those predicted by camera models across the detector based on pixel spacing, focal length, and distortion coefficients. In the analysis the desired measurements are the pixel locations (samples) of identifiable locations in the bar patterns. We chose the left sides of up to five bars to the left of the fiducial and one bar to the right. The edge was determined using existing software for measuring limb coordinates of objects that models a Gaussian decrease of signal from a sharp edge. For bars close to the fiducial the out-of-focus character gave a spread somewhat greater than the software was nominally adjusted to, and as is noted below, some data had uncertainties of more than a half pixel and were thus excluded. This did not substantially impact the spread of useful data across the detector. This relatively narrow-angle device does not require complex functions for distortion description. The basic geometry is shown in Fig. 16. Here $xc/fl = \tan(\alpha)$, where xc is the mm coordinate of the undistorted image, and fl is focal length in mm, and α is the angle from the optical center.

A simple quadratic distortion correction is given by Davies et al. (1994):

$$xd = xc \cdot (1 + k \cdot r^2),$$

where xd is the distorted position (the actual measured position), k the distortion coefficient, and r is the distance from the optical center (the difference in samples from the optical

Fig. 16 Idealized camera geometry. Here $xc/fl = \tan(\alpha)$, where xc is the mm coordinate of the undistorted image, and fl is focal length in mm, and α is the angle from the optical center

center). In this one-dimensional case, offset of the true optical center from the line array cannot be measured, and would largely affect the value of the distortion coefficient. The undistorted coordinates thus are:

$$xc = \frac{xd}{1 + k \cdot r^2}.$$

For any combination of focal length, optical center position, and distortion coefficient we can calculate left and right sample coordinates for 1 degree changes in α across the entire field of view. We choose to measure this difference as right (greater) sample − left (lesser) sample, and thus are able to tabulate this difference for samples up to 5000 samples minus the one degree difference in samples, or roughly from sample 1 to sample ∼3200. Our fit is made by comparing the observed one degree difference in samples versus the predicted value for the (left, low-pixel) samples tabulated. Residuals are the predicted minus observed number of samples, and the best fit is taken at minimum root mean square of the residuals.

It is assumed that the detector lies in the plane of rotation of the stage. If the detector is tilted relative to this rotation, a given angular rotation will result in a larger change in position on the detector, which would result in a larger calculated focal length. Review of the mechanical arrangement indicates possible misalignment of $0.88 \pm 0.1°$. Error induced across the field of view from this would be ∼0.8 pixels. We choose to leave the numbers uncorrected.

The fitting result for NAC-L is displayed in Fig. 17. The resulting distortion coefficients and optical center position for both cameras are included in Table 2.

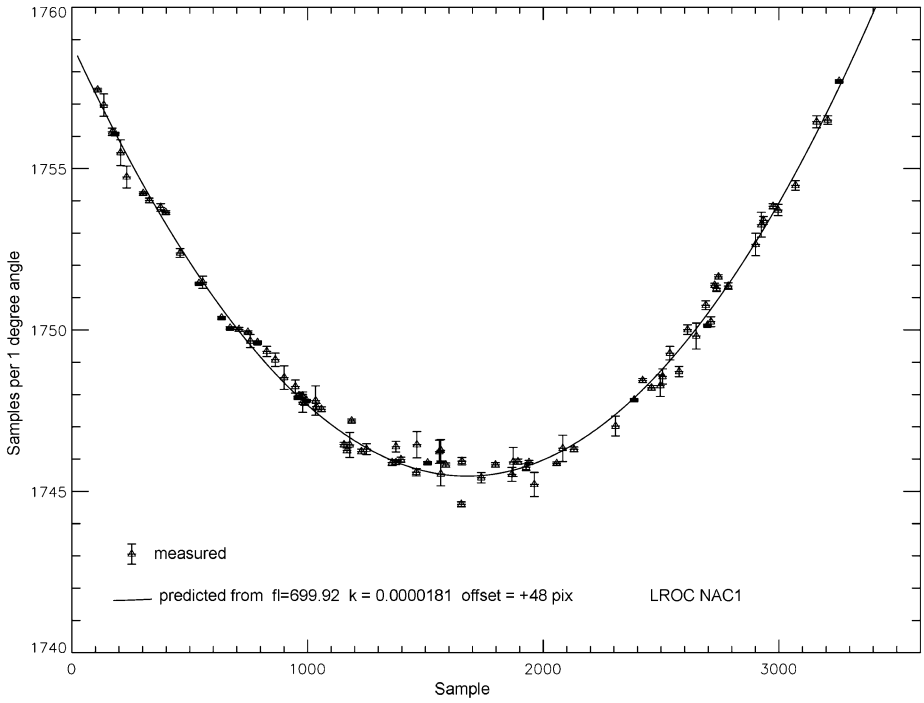

Fig. 17 Fitting results for NAC-L. Offset is distance of optical center from sample 2500

4.1.9 Stray Light Measurements

To search for stray light effects, the beam of the QTH calibration lamp was aimed directly into the NAC's aperture at various angles (up to about 60 degrees in the crosstrack direction only). A photo of this setup is shown in Fig. 18. No light leaks and no large-angle stray-light problems were identified. However, two out-of-field low-level stray light features were detected affecting the pixels centered at samples 1000 and 4000. These features were further quantified with two setups: (a) an integrating sphere illuminated with a QTH lamp was moved perpendicularly to the camera's line of sight, with small increments centered around an angle of about 5°; (b) the flat-field images described in Sect. 4.2.5 were compared with flat-field images where increasingly large parts of the Spectralon panel were covered with black panel (a photo of this setup is shown in Fig. 19). Both the NAC-L and NAC-R stray light features have magnitudes of 1–3% of a uniform flat field wide enough to include the entire out-of-field source of the stray light (Fig. 20). The test data acquired is sufficient to fully characterize and develop a mitigation strategy if necessary.

Additionally, with no ambient illumination a high intensity focused flashlight beam was held adjacent to all structural seams and fasteners for both the telescope and electronics housing (both NACs) while long integration images were acquired. This test revealed no light leaks.

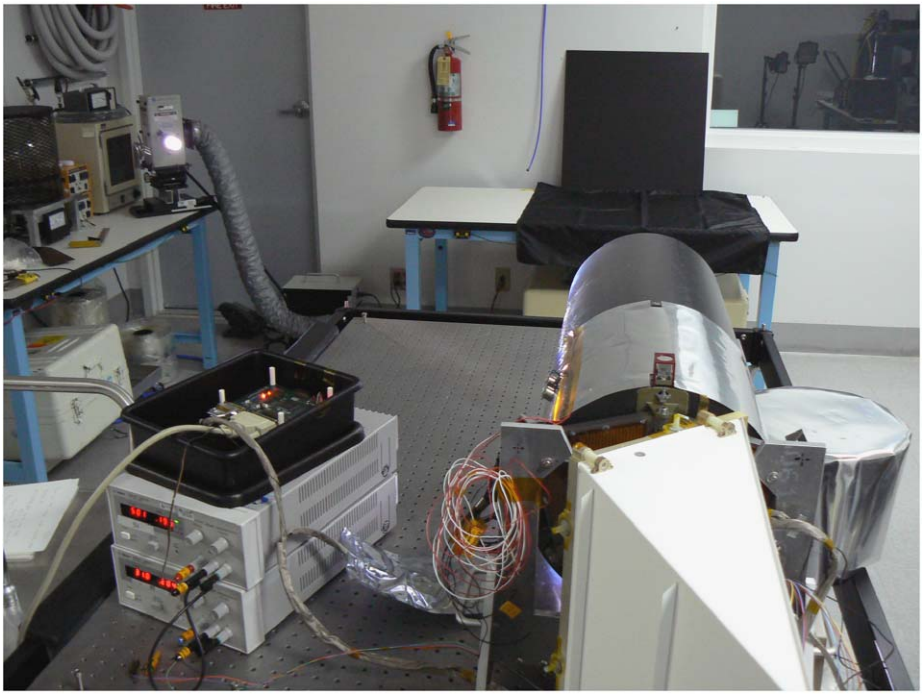

Fig. 18 NAC stray light test setup. The quartz tungsten halogen lamp in the back-left corner was moved perpendicularly to the line of sight between the NAC (right foreground) and the black plate on the wall while rotating the lamp such that it pointed at the telescope aperture

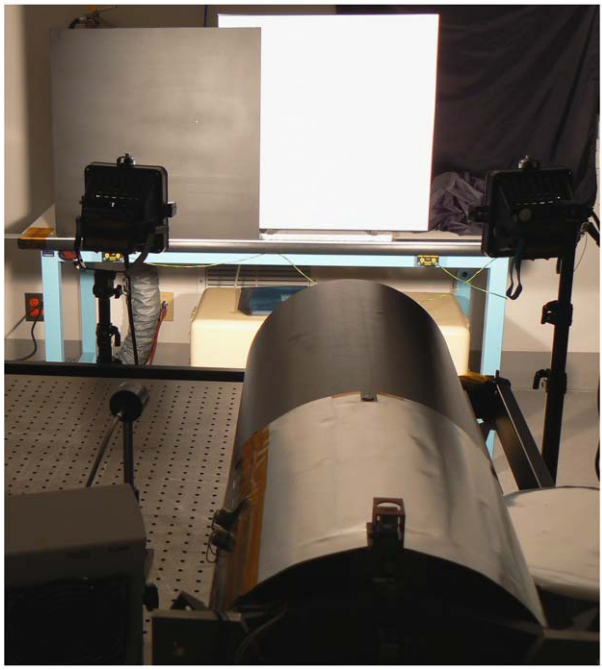

Fig. 19 Setup for characterization of the NAC out-of-field stray light. The NAC (foreground) viewing a Spectralon panel (*white*) illuminated by studio lamps. In the experiment a black plate (*left*) is moved with one inch (2.54 cm) increments across the spectralon panel

4.1.10 Focus Test

The NAC carbon-fiber structure absorbs water under ambient conditions resulting in expansion that in turn affects focus. Thus accurate measures of focus must be performed after baking out the telescopes in a vacuum environment. Focus verification was performed during environmental testing by imaging a tilted bar target mounted at the focus of a collimator built with optics identical to that of the NACs. Measured MTFs were above requirement (0.2 at Nyquist) for both NACs across the full range of telescope operating temperatures. Shortly after removing each NAC from the vacuum chamber the Moon was imaged as a qualitative focus check (Fig. 21). Comparison of the moon image with an equivalent CTX image, and analysis of the limb to space edge, indicates both NACs to be in focus. A quantitative measure of focus from the lunar images is not useful due to less than optimal seeing conditions and hand scanning.

4.2 WAC Calibration

4.2.1 Detector Characterization

The detector gain, read noise, and full-well were calculated using the photon transfer method (Janesick 2007). The setup for this experiment consisted of a Xenon lamp illuminating a 10″ (25.4 cm) diameter integrating sphere with a 4″ (10.16 cm) diameter exit portal. Three sets of linearity images were taken, for each set the exposure times ranged from zero ms to sufficiently long exposures to saturate all filters. After background subtraction the total noise, read-plus-shot noise, and the shot noise are plotted versus the signal (Fig. 22). The measured gain, read noise and full well are listed in Table 3. Errors were estimated by varying the input parameters (boundary of the linear fit and the determination of the read noise). The

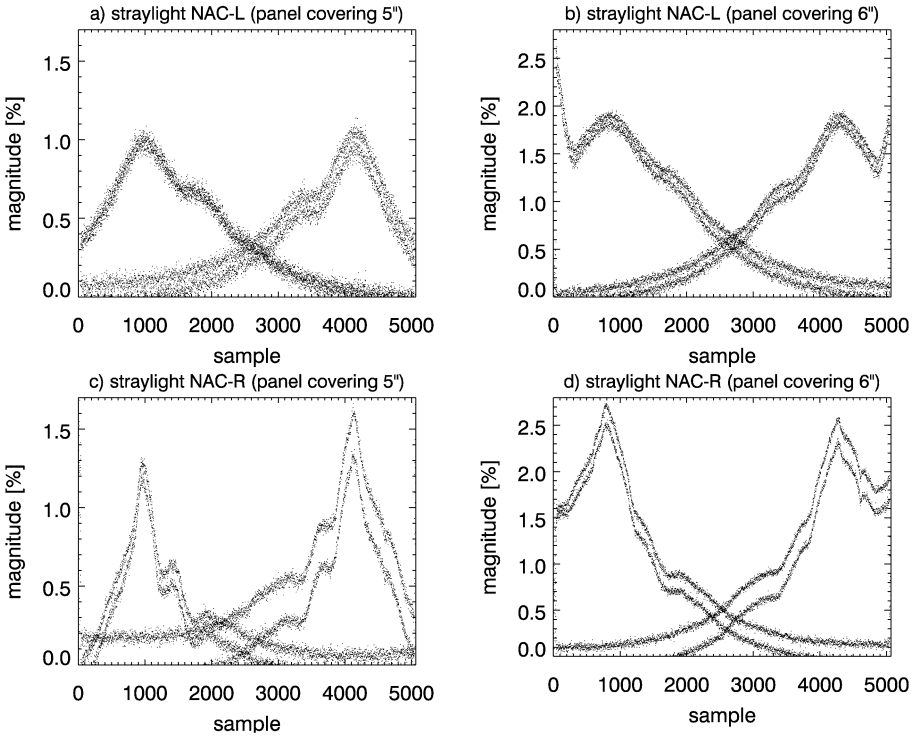

Fig. 20 The magnitude of the NAC stray light features was determined by dividing normal flat-field images with those where parts of the Spectralon panel were covered with a black panel. Here the unit is this ratio minus 1, given in percent. **a** and **b**: NAC-L results with the black panel covering 5″ (12.7 cm) and 6″ (15.2 cm) of the Spectralon panel. **c** and **d**: NAC-R results with the black panel covering 5″ (12.7 cm) and 6″ (15.2 cm) of the Spectralon panel. The two distinct populations represent even and odd pixels

WAC CCD has a highly linear response between 5% and 90% of the saturation value (see Fig. 23). Around 1800 DN the sensor behaves in a non-linear manner.

4.2.2 WAC Calibration Pipeline

The calibration to radiance or I/F is a standard procedure described by:

$$I_{cal}(x, y, f, \tau, T) = \frac{I_{raw}(x, y, f, \tau, T) - D(x, y, f, \tau, T) + N(x, y, f)}{F(x, y, f) \cdot \tau \cdot r_f},$$

where

$I_{cal}(x, y, f, \tau, T)$ is the calibrated signal of the pixel at position (x, y) in radiance units of µW/(cm^2·sr·nm),
$I_{raw}(x, y, f, \tau, T)$ is the pixel's raw signal in DN,
f is the filter,
τ is the exposure time,
T is the temperature,
$I_{raw}(x, y, \tau, T)$ is the raw signal in DN,
$D(x, y, f, \tau, T)$ is the dark image,

Fig. 21 NAC-L image of the Moon obtained immediately after removing instrument from thermal vacuum testing. Slight deviations from sphericity are due to scanning the NAC by hand, Moon is about 940 pixels in diameter

$N(x, y, f)$ is non-linearity correction (term above 1600 dn)
$F(x, y, f)$ is the sensitivity non-uniformity correction matrix (flat-field), and
r_f is a filter's responsivity coefficient to convert DN to radiance

The individual steps are discussed in detail in the following sections. The flowchart provided as Fig. 24 provides a graphical illustration of the WAC calibration pipeline. The WAC data are first decompressed. The subsequent conversion from 8-bit to 11-bit data follows the inverse of the conversion look-up-table presented in Fig. 25.

4.2.3 Background Characterization

For the WAC, unlike the NAC, it is in principle possible with the WAC to remove the electronic bias by taking dark images with 0 ms exposure. Yet unlike the NAC electronics it is not possible to change the bias level by simply uploading a parameter on a per image basis, but rather the bias is a fixed value in the flight software and can only be changed with a flight software modification. In the calibration pipeline (Sect. 4.2.2) the total background, which includes the bias, is removed from the scene image in one step. To characterize the dark signal dependence on exposure time and temperature, a comprehensive set of images was acquired during thermal vacuum tests over a range of temperatures (−40°C to +25°C) spanning expected flight conditions (Fig. 26).

4.2.4 Linearity Correction

Above 1800 DN (background corrected) the WAC response is non-linear (Fig. 23). For background corrected values between 1800 and 1950 a linearity correction is applied by

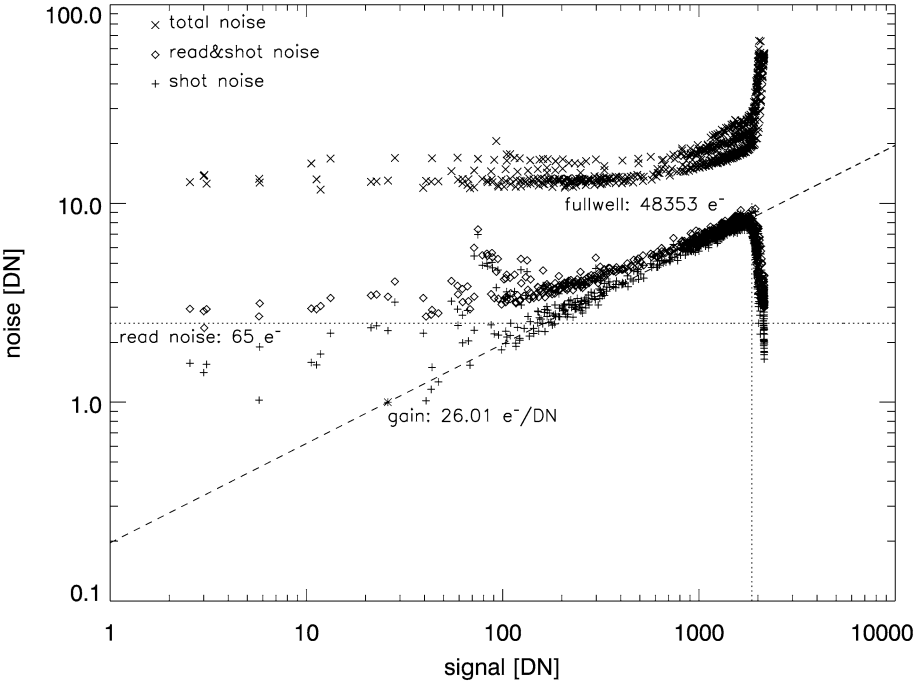

Fig. 22 WAC Photon transfer curve. The linear fit of the shot noise between signal levels of 500 DN and 1600 DN yields a gain of 26.0 e^-/DN. This value is within the uncertainty range of 0.7 e^-/DN (around an average of 25.9 e^-/DN), which was estimated by varying the endpoints of the linear fit range, the number of pixels used for analysis, and the determination of the read noise

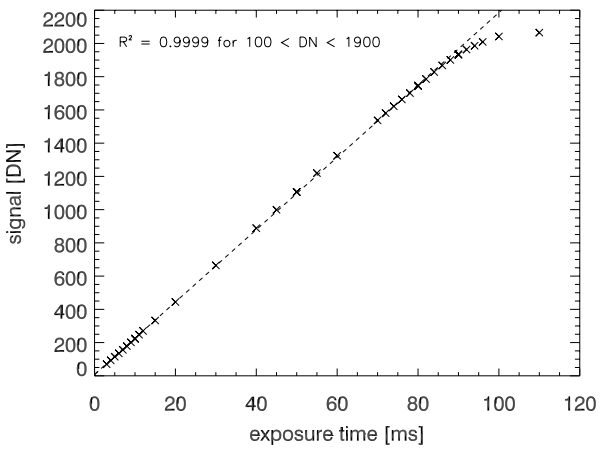

Fig. 23 WAC linearity measurements for the 645 nm band. The system response is highly linear until ∼1800 DN (background corrected)

elevating a particular DN to match corresponding line fitted from the linear range. Above 1950 the data are considered saturated and thus not useful for quantitative analysis.

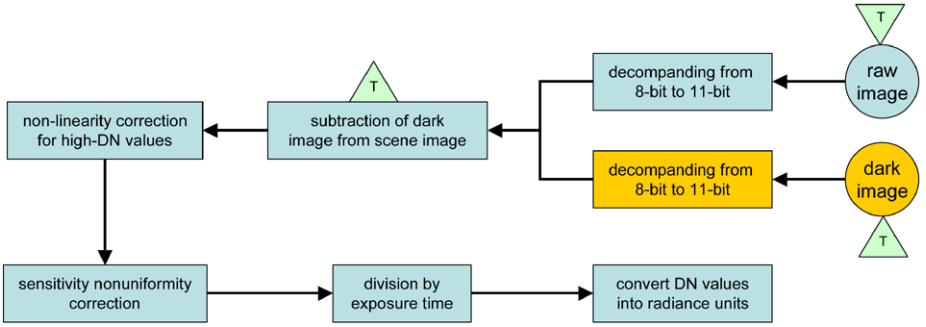

Fig. 24 Schematic overview of the WAC calibration pipeline. Depending on the electronics temperature "T," images have a different background level (bias plus dark current), which is subtracted with the corresponding dark image. The non-linearity for high-DN values is corrected, as well as the sensitivity non-uniformity (flat-fielding). The final steps are the division by exposure time and the conversion into radiance units

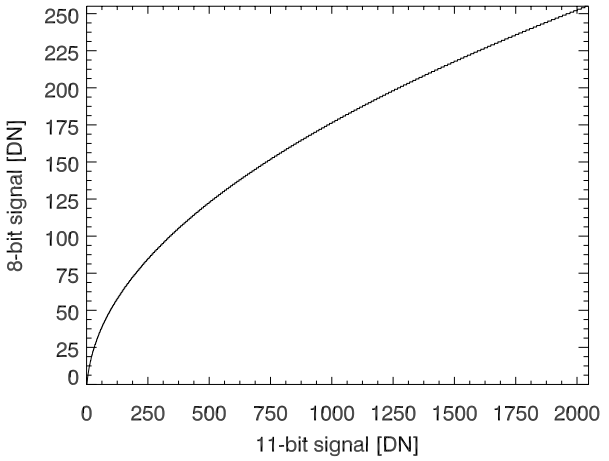

Fig. 25 Graphic representation of the WAC companding scheme (11-bit to 8-bit)

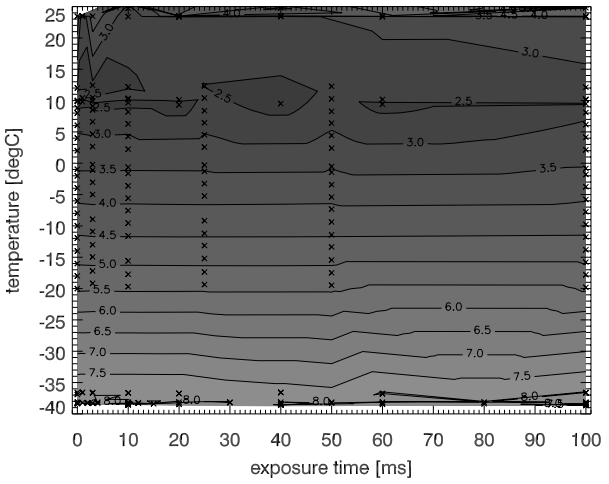

Fig. 26 WAC dark signal (contour lines) raw DN as function of exposure time [ms] and temperature [°C]

Fig. 27 Non-uniformity matrix of the 5 visible filters (415 nm band to 690 nm band, top to bottom). The *red shading* is not part of the system response but rather delimits portions of the CCD readout in multispectral mode. Monochrome images are acquired with the 645 nm filter (4th band from top)

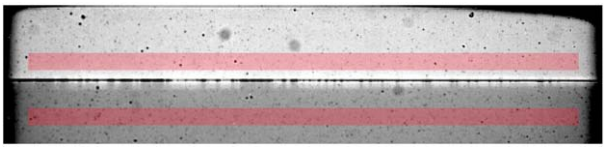

Fig. 28 Flat-field image of the two UV filters (*top*: 320 nm; *bottom*: 360 nm). The areas shaded in *red* are used for the actual imaging; note that 4 × 4 binning has not been applied to the data shown here

4.2.5 Sensitivity Non-uniformity Correction

The wide angle FOV (90°) of the WAC was much larger than the aperture of the available integrating sphere thus the sensitivity non-uniformity was characterized through a series of images. The WAC was rotated through 98 degrees such that every three degrees an image of the sphere aperture was acquired. The central portion of these images were mosaicked to construct the final sensitivity non-uniformity matrices (Figs. 28, 29). This method is identical to that described in Bell et al. (2009).

4.2.6 Spectroradiometric Calibration

The full system spectral response of the WAC was first characterized with a monochromator illuminated with a calibrated Xenon light source. Two tests were performed with the monochromator illuminating discrete spots on each filter. First, out of band leaks for each filter were tested by stepping through the full spectral sensitivity of the detector (250 nm to 1100 nm) at 10 nm steps with 100× overexposures. Out of band leaks were shown to be less half a percent in all visible bands (at a single point on each filter). To test if any of the visible filters suffered from spatially variable out of band leaks a series of images (5 second exposures) were taken through narrow band filters (420 nm ± 5 nm, 550 nm ± 5 nm, 600 nm ± 5 nm, 650 nm ± 5 nm, 750 nm ± 5 nm) placed in front of the Xenon lamp illuminating the integrating sphere. These images indicated no out of band leaks, though we note this test did not test the full spectral sensitivity range of the CCD. Therefore it is concluded that all filters have a maximum out-of-band leak of less than 0.5%.

Characterizing the system sensitivity profile for each filter was next accomplished by stepping the monochromator through 2-nm increments across a given filter's full spectral width. The projected image of the monochromator spot exhibited Gaussian brightness contours with the peak area being on the order of the size of a pixel. As the monochromator was adjusted in wavelength (2-nm steps) the location and shape of the spot changed while drifting across the sensitive area of the center pixel. Thus accurate in-band spectral response proved to be problematic due to the unfavorable pixel fill factor (20%) of the KAI-1001.

Final characterization of the band sensitivity was ultimately accomplished by calculation from the vendor supplied measurements of the individual components (optics with coatings, filters, CCD quantum efficiency). The estimated WAC filter bandpasses are summarized in

Table 4 WAC filter bandpasses and responsivity coefficient (RC)

Band name	λ_{eff} [nm]	FWHM [nm]	RC [(W/m^3/sr)/(DN/s)]
320 nm	321	32	865
360 nm	360	15	918
415 nm	415	36	3727
565 nm	566	20	3310
605 nm	604	20	3377
645 nm	643	23	3273
690 nm	689	39	2612

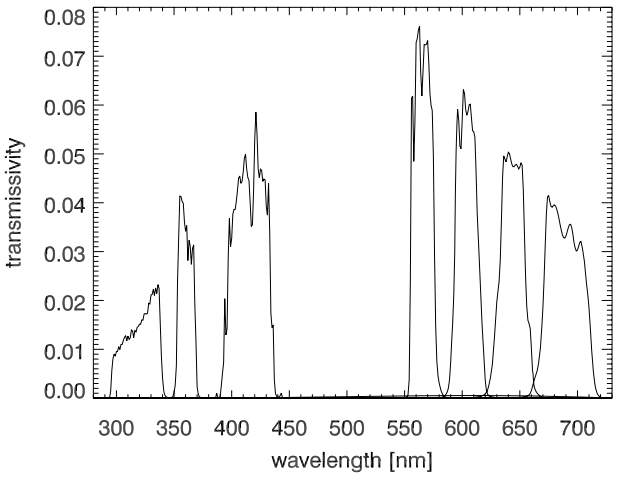

Fig. 29 Estimated spectral system throughput of the seven WAC bandpasses

Table 4 and their spectral transmissivities are displayed in Fig. 29. Images of a color standard were acquired by tilting the WAC through a series of angles to build up a complete scan. These data were background corrected and flat-fielded to check for low frequency flat field residuals, pinholes, and undetected out of band leaks (Fig. 30), no problems were detected.

4.2.7 Absolute Calibration

With the knowledge of the WAC system spectral response and the radiometric source calibration the system spectral responsivity in units of (DN/s)/(μW/(cm^2·sr·nm)) is calculated for each filter (Table 4). For the independent determination of each filter's signal-to-noise ratio (SNR) the dark-subtracted images of the photon transfer curve analysis (Sect. 4.2.1) were analyzed. Due to the fixed-pattern-noise correction with flat-field images the remaining noise for the calculation is the read-plus-shot noise. Thus the SNR is calculated as the signal divided by the read-plus-shot noise in a selected "clean" area of each filter. Above 1000 DN the SNR is ∼150 for the UV and visible bands (Fig. 31).

4.2.8 Geometric Calibration

Geometric calibration was performed by mounting the WAC on the Ultradex rotary stage for "azimuthal" control in 1-degree steps, with elevation separately provided by another rotary

Fig. 30 WAC RGB composite (RGB: 689, 643, 415 nm) of standard Munsell Color chart and geologic samples

stage with continuous variability. The one degree rotation steps provided by the Ultradex stage are accurate to less than 1-arcsecond; the elevation rotations are not as accurate; they are checked in the analysis. The target is a collimated spot image of selectable size. Illumination is by a QTH lamp with a collimating lens illuminating the pinhole for the visible images, a Xenon lamp with a collimating lens illuminating the pinhole for the UV images. The resulting images, one each for every azimuth and elevation of the collimator, provide spots spread over a few pixels width. Existing centroiding software provided the lines and sample of spot centers, from which the detector mm coordinates were recorded. The goal is to provide a function relation between line and sample in the detector and viewing angles from the camera.

Due to its wide field-of-view the WAC exhibits more distortion than the NAC, thus an additional distortion term is required:

$$xd = xc \cdot (1 + k_1 \cdot r^2 + k_2 \cdot r^3),$$

$$yd = yc \cdot (1 + k_1 \cdot r^2 + k_2 \cdot r^3).$$

For the visible detector, $k_1 = -0.0099$, and $k_2 = -0.00050$. For UV detector, $k_1 = -0.024$, and $k_2 = -0.0070$. The resulting focal length and FOV solutions are given in Table 3.

4.2.9 Stray Light Measurements

A discrete collimated point source was rastered in and out of the WAC Visible FOV to check for glints and scattered light (Fig. 32). The collimated beam (pinhole 0.1 cm) formed a circle of light ~3 pixels in diameter (FWHM) at unsaturated exposure levels. For each position 100× and 600× over-exposed images were acquired to check for low level effects. Measurable effects were only found on one side of the detector (Fig. 33). During lunar imaging the first 20 to 40 columns will suffer from scattered light contamination approximately 5 to 10% of scene brightness during monochrome full field imaging. No scattered light was detected in the multispectral readout zone.

In the darkened calibration facility a high intensity focused flashlight beam was held adjacent to all structural seams and fasteners for both the optics and electronics housings while long integration (1000 ms) images were acquired. This test did not reveal any light leaks.

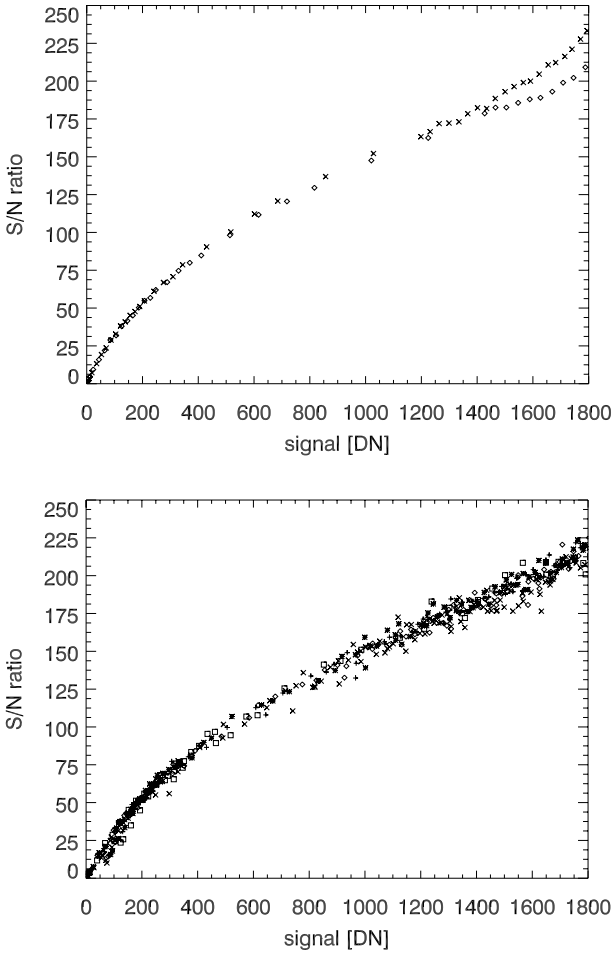

Fig. 31 (*Top*) The SNR for the two UV bands: 320 nm (*crosses*)/360 nm (*diamonds*). (*Bottom*) SNR estimates for the five visible bands: 415 nm (*crosses*)/565 nm (*diamonds*)/605 nm (*plus-signs*)/645 nm (*asterisks*)/690 nm (*squares*)

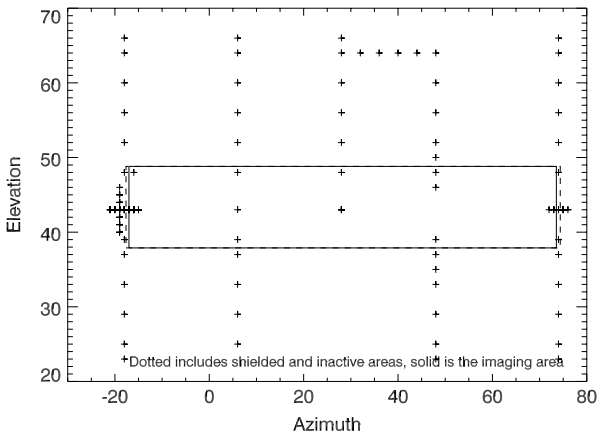

Fig. 32 Schematic showing approximate locations of collimated light beam in WAC 1 (not the flight unit) stray light testing, similar test results were obtained from the flight unit

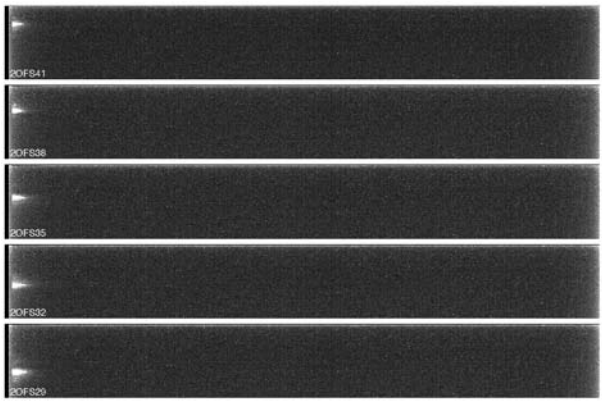

Fig. 33 WAC 1 (not the flight article) frames showing glare artifact when collimated source was moved vertically outside field of view, similar results were obtained with the flight WAC. Exposure time was ∼600× that of normal exposure. At normal exposures levels the glare peaks at about 20 DN above background and affects the first 20 imaging columns

5 LROC Operations

The LROC Science Operations Center (SOC) is located at the School of Earth and Space Exploration at Arizona State University in Tempe, AZ. All LROC uplink, downlink, processing, and archival activities take place at this state-of-the-art facility. The LROC SOC supports LROC operations through all phases of the LRO mission. In this section, we provide a brief overview of LROC Operations.

5.1 Data Volume

The SOC accommodates LROC's ∼400 Gbits of data downlink per day with lossless compression, which will produce a total of almost 30 terabytes (TB) of raw data over the nominal mission. Production of higher-level data products will eventually produce a total of $>$ 100 TB for archive in the Planetary Data System (PDS).

5.2 Software

To reduce schedule risk and cost, LROC is leveraging existing software to the fullest practical extent. Brief summaries of the software packages deployed by the LROC Operations Team to support mission goals are provided below.

5.2.1 REACT

The LROC Science Team populates a planning database with NAC targeting requests using the Rapid Environmental Assessment Composition Tools (REACT) planning tool. REACT was developed by Applied Coherent Technologies (ACT) as a generic spacecraft remote-sensing target planning tool and is also used operationally by other spacecraft instrument teams including Chandrayaan-1's Moon Mineralogy Mapper, MESSENGER, and the Mars Reconnaissance Orbiter's Compact Reconnaissance Imaging Spectrometer. REACT is a GIS-based application that allows the user to specify Regions of Interest (ROIs) using various lunar global basemaps. Target-request ROIs entered into the database through REACT are defined as points, lines, or polygons and contain specific acquisition parameters such as lighting (high sun or low sun), percent coverage, repeat observations, and resolution. ROIs specified by the Science and Operations Teams are uploaded to a central database on the ACT server. The targeting strategy is discussed in detail in Sect. 5.3.1.

5.2.2 JMoon

JMoon (JMars 2010) is a derivative of the Java Mission-Planning and Analysis for Remote Sensing (JMARS) software, the observation and planning tool that was developed to support the Mars Odyssey THEMIS experiment. JMoon uses the spacecraft's predict ephemeris to determine the LROC observing opportunities that lie under LRO's orbit track, allowing analysts to interactively select and position LROC NAC targets from the target request database created by the LROC Science Team. The LROC Operations Team uses JMoon to convert the ROIs created by the LROC Science Team in REACT into the command loads sent to the instrument in flight.

5.2.3 AutoTarget

AutoTarget is a tool developed by the LROC Operations Team designed to facilitate the automated generation of LROC command loads. AutoTarget automatically creates LROC command loads using the LRO predict ephemeris to locate targets in the LROC target request database or by randomly placing NAC targets where no target requests are available. AutoTarget is used for specific LROC targeting functions, including random observations along a complete orbit track, planning observations for the global or polar mapping campaigns, and pairing complementary stereo or mosaic observations with existing observations.

5.2.4 CommandGen

Once the LROC Operations Team has completed an observational plan, the software tool CommandGen (short for **Command Gen**erator) collects the details of all the planned observations for the given orbit window and compiles them into command load files. These CommandGen products are then sent to the LRO Mission Operations Center (MOC) at the NASA Goddard Space Flight Center for integration with the LRO command load and subsequent uplink to the spacecraft.

5.2.5 LROC Database

The LROC SOC uses PostgreSQL 8.3 to store data accumulated and created during LROC operations. PostgreSQL was chosen due to its extensive and mature feature set, including robust transaction logging, foreign key relationships, point-in-time recovery, and its demonstrated ability to handle large volumes of data under heavy load. The database will support LROC operations both by providing an archive of the data produced during operations and also by providing data storage and retrieval services (session management) for all aspects of LROC data processing. The LROC Database will facilitate creation of PDS deliveries by pre-packaging all pertinent information prior to the PDS delivery process. The LROC database natively supports geographic objects and functions, enabling the LROC SOC to store and produce OpenGIS compliant data products.

5.3 Concept of Operations

Here, we provide an overview of the concept of operations for the LROC Science and Operations Teams during the LRO nominal mission. These operations include science targeting, operational target definition, operational target selection, command sequence generation, transfer of downlinked image data, data processing, special product generation, and data archiving.

5.3.1 LROC Science Targeting Request Process and Strategy

LROC NAC science target requests are generated by the LROC Science and Operations teams interactively using the REACT software package (Sect. 5.2.1) and are organized in several ways, the most important of which is target priority. The priorities are as follows:

(1) Exploration targets requested by NASA's Project Constellation
(2) Targets that fulfill other LROC Level 1 Requirements (detailed in Sect. 2)
(3) Targets that support LROC Science Team and LRO mission science objectives
(4) Science requests from outside the LRO team
(5) Public target requests

During the first year of the LRO mission, the Priority 1 targets consist of sites specified by the NASA Constellation Project. These sites were selected on the basis of scientific, resource utilization, and operational merits as well as a desire to span the range of lunar terrain and geologic features, including polar sites, mare and cryptomare surfaces, pyroclastic deposits and other volcanic landforms, impact basins and crater terrains, locations with representative rock-type exposures, and unusual features such as radar anomalies, magnetic anomalies, albedo swirls, sites of possible outgassing, and compositional anomalies that have been observed from orbit. The Priority 1 targets are derived primarily from three reference target sets (1) The ten design reference sites listed by the 2005 Exploration Systems Architecture Study, (2) the six sites evaluated by the 1991 *Site Selection Strategy for a Lunar Outpost* workshop for the First Lunar Outpost study, and (3) the 59 sites identified by the 1988 workshop on *Geoscience and a Lunar Base: A Comprehensive Plan for Lunar Exploration* (Taylor and Spudis 1990; NASA 2005, 1990).

The LROC Science Team is also generating a comprehensive set of NAC high-resolution image acquisition target requests that achieve LROC measurement objectives, science objectives proposed by the LROC participating scientists, and targets relating to features of generally known geologic interest. These targets include, but are not limited to, spectral anomalies (Wood and Head 1975), Copernican craters (Wilhelms et al. 1987), Apollo Panoramic photo areas (Masursky et al. 1978; Lawrence et al. 2008b), crater central peaks and peak rings, sites of lunar pyroclastic volcanism (Gaddis et al. 1985, 1995, 2000, 2003), lava flow margins (Gifford and El-Baz 1981), possible lava tubes (Coombs and Hawke 1992), mare surfaces for crater counting (Hiesinger et al. 2003), volcanic domes (Head and McCord 1978), geologic units in the Apennine Mountains and Imbrium backslope (Wilhelms 1980; Wilhelms et al. 1987), tectonic structures, dark haloed impact craters and cryptomaria (Blewett et al. 1995; Giguere et al. 2003, 2007; Hawke et al. 2004, 2005, 2007, 2008; Lawrence et al. 2008b), concentric craters (Wood 1978), sites of observed impact flashes (Ortiz et al. 2000, 2002, 2006; Yanagisawa and Kisaichi 2002; Cudnik et al. 2003), and highland scarps.

5.3.2 Operational Target Definition

The LROC SOC uses the software tools described in Sect. 5.2 to plan observations and generate command loads for the NAC and WAC on a daily basis. Based on the most recent predicted LRO spacecraft ephemeris (which will be received and updated daily from the LRO MOC) and the NAC Target Request Database for upcoming orbits, an operations plan for the next 72 hours of normal operations will be generated and submitted to the LRO MOC each day. The NACs can be commanded individually or together, and in normal operating mode can acquire images of any length in 1024-line increments up to the full length of

52,224 lines with a maximum of 15 NAC image-pairs of the illuminated surface possible per orbit, for a theoretical daily total of 180 NAC pairs (or 360 images). Each LROC operational plan will therefore include NAC requests for at least 1000 images. Before NAC images are written to the spacecraft's solid-state data recorder, they are temporarily stored in a 256 MB buffer. It takes approximately 15 seconds to acquire a full NAC image pair and another 220 seconds to read that image pair through the SCS to the LRO solid-state recorder. It is not possible to obtain another NAC image until the buffer is cleared, so after the collection of each NAC pair there is an 11° down-track latitude zone where additional imaging cannot be acquired. In addition to NAC commands for target requests, each 3-day plan will also include commands for the WAC. The WAC is not buffer limited and will almost always be imaging when over the daylight side of the Moon.

5.3.3 Spacecraft Slews

The daily target plans include on average three off-nadir spacecraft roll (up to 20°) observations per 24-hour period and any number of slews 2° or less, barring no operational conflicts. More than three slews greater than 20° per day are not permitted in order to minimize disruption to the other LRO science instruments. Off-nadir slews are necessary to fulfill stereo and mosaic requests. Geometric stereo requires two images of the same terrain with a 10–50° angle between the two observations with respect to the target and incidence angles as similar as possible ($< 20°$ difference). Photometric stereo requires three or more images of the same terrain, with each observation in the set differing by at least 20° in incidence and azimuth angles from one another. Instrument slew maneuvers for star calibrations, limb views, 90° yaw offset, or slews $> 20°$ are specially planned in advance due to the operational complexity and disruption to normal mapping for the payload suite.

5.4 In-flight Calibration

Comprehensive in-flight calibration sequences are planned for the operational phase of the LRO mission. Details for both the NAC and WAC subsystems are provided below.

5.4.1 LROC NAC Calibration Imaging

The NACs will acquire images on the lunar farside during non-illuminated periods in order to characterize the dark current behavior of the CCDs. This operation is not possible while the spacecraft is on the night-time nearside because of Earth-shine. During the initial cruise to lunar orbit (0–3 days after the launch), the NACs will image open space while the Moon is: (1) far from the edge of the field of view (2) near the edge of the FOV and (3) within the FOV. This series of observations will be used to characterize stray light within the NAC instruments.

5.4.2 LROC WAC Calibration Imaging

Calibration images will be obtained with the WAC during the cruise phase by imaging the Earth and Moon, both inside and outside of the instrument's imaging field of view. The imaging of point-sources such as stars and nearby planets will also be performed. In the 50-km nominal mission orbit, image calibration will typically include the acquisition of images on the non-illuminated far side of the Moon for dark reference calculation and the regular imaging of select stars and planets.

Table 5 LROC data measurement sets

Measurement Set	Estimated Storage Allocation (GB)	Pixel Scale (m/pixel)	Product Description
EDR/CDR	60,000	0.5 to 100	Level 0, Level 1A (EDR,CDR)
SPECIAL DATA PRODUCTS TO SATISFY LROC MEASUREMENT OBJECTIVES			
Landing Site Certification	500	0.5	50 Hi-priority uncontrolled site mosaics
Synoptic Polar Illumination	179	100	2 Polar movies, Illumination Maps
Meter Scale Polar Illumination	293	1	2 Summer uncontrolled mosaics
High-resolution topography	25	1–10 (vertical)	Select DEMs, Co-registered sets
Global Multispectral	639	100	Select uncontrolled mosaics
Global Black-and-white Basemap	27	100	Uncontrolled mosaics
Regolith Investigation	128	0.5	Catalog, Mosaics
Recent Small-impact rate	1280	1	Catalog, Sample co-registration sets
Total: 63,017 GB			

5.5 LROC Downlink Operations

Spacecraft downlink will occur during S-band (256 kbps, for housekeeping) and Ka-band (100 Mbps, for image data) contacts. The MOC will provide the LROC SOC with access to real-time housekeeping telemetry in order to allow monitoring of instrument operations and health. In general, there will be an average of four Ka-band contacts per day and at minimum one 30-minute S-band contact per orbit. Up to 15 NAC pairs/orbit can be accommodated given sufficient downlink bandwidth, for a total of approximately 180 NAC pairs per day.

The instrument data files returned from the spacecraft first arrive at the MOC and are then sent to the SOC. As the raw LROC data files arrive at the SOC, they are validated, queued for image processing and reduction, processed, and archived with the PDS. An enterprise-grade storage array at the SOC will provide 200 TB for production-file storage. LROC image processing will be done using Linux servers running ISIS software to generate PDS data products (EDRs, CDRs, and RDRs see Sect. 5.5.1.1). Image processing is pipelined using the Rector software, which has been self-developed by the LROC Operations Team. Rector automates the data processing steps by controlling product migration through a series of scripts across networked machines. Failures in the data processing pipeline will be recorded for resolution. There are no manual steps in the pipeline (except when failures arise) in order

to mitigate time-intensive tasks associated with the processing of the large volume of LROC data received daily during the nominal mission.

5.5.1 Data Products

5.5.1.1 EDRs and CDRs LROC's key data products are the documented, verified PDS-format Experiment Data Records and Calibrated Data Records. These products form the basis of all Reduced Data Records (RDR) produced in order to extract scientific information from various measurement data sets. RDRs might include: image cubes of multispectral data, mosaics of multiple images, DEMs, perspective view maps, and various color composites. All RDRs are produced on a best-effort basis, using the United States Geological Survey's ISIS image processing software (USGS 2010) in a geometrically uncontrolled format to support the LROC measurement goals. The LROC RDRs that will be generated to fulfill the LROC proposed measurement objectives are detailed in Table 5.

Acknowledgements We thank the many contractors who helped bring LROC to realization. This paper was improved by comments from two anonymous reviewers.

Appendix A

NAC bit-compression tables (from 12-bit to 8-bit data):

NAC images are companded using a piecewise linear transfer function with up to five segments. The companding scheme can be described as linear functions with corresponding segments defined by 12-bit DN ranges. Note that the y-values (8-bit) are always truncated.

Code 0: NAC nominal table (square-root-like)

	linear function	12-bit DN range (y)	8-bit DN range (x)
Segment 1	$y = 1/2 \cdot x + 0$	0–31	0–15
Segment 2	$y = 1/4 \cdot x + 8$	32–135	16–41
Segment 3	$y = 1/8 \cdot x + 25$	136–542	42–92
Segment 4	$y = 1/16 \cdot x + 59$	543–2206	92–196
Segment 5	$y = 1/32 \cdot x + 128$	2207–4095	196–255

Code 1: NAC lin1 (0 DN to 255 DN mapped one-to-one)

	linear function	12-bit DN range (y)	8-bit DN range (x)
Segment 1	$y = x$	0–255	0–255
Segment 2	$y = x - 256$	256–510	0–254
Segment 3	$y = 1/32 \cdot x$	511–4095	15–127

Code 2: NAC lin16 (12 bit to 8 bit linear)

	linear function	12-bit DN range (y)	8-bit DN range (x)
Segment 1	$y = 1/16 \cdot x$	0–4094	0–255
Segment 2	$y = 1/32 \cdot x$	4095–4095	127–127

Code 3: NAC low signal table (optimized for DN < 500)

	linear function	12-bit DN range (y)	8-bit DN range (x)
Segment 1	$y = 1/2 \cdot x + 0$	0–63	0–31
Segment 2	$y = 1/4 \cdot x + 16$	64–423	32–121
Segment 3	$y = 1/8 \cdot x + 69$	424–535	122–135
Segment 4	$y = 1/16 \cdot x + 103$	536–799	136–152
Segment 5	$y = 1/32 \cdot x + 128$	800–4095	153–255

Code 4: NAC high signal table (optimized for 500 < DN < 2000)

	linear function	12-bit DN range (y)	8-bit DN range (x)
Segment 1	$y = 1/8 \cdot x + 0$	0–1039	0–129
Segment 2	$y = 1/16 \cdot x + 65$	1040–1999	130–189
Segment 3	$y = 1/32 \cdot x + 128$	2000–4095	190–255

Code 5: NAC cap Nq/Ne table (minimize quantization noise for low DN)

	linear function	12-bit DN range (y)	8-bit DN range (x)
Segment 1	$y = 1/4 \cdot x + 0$	0–111	0–27
Segment 2	$y = 1/8 \cdot x + 14$	112–815	28–115
Segment 3	$y = 1/16 \cdot x + 65$	816–1999	116–189
Segment 4	$y = 1/32 \cdot x + 128$	2000–4095	190–255

Simply inverting the companding equations allows the 8-bit value to be decompanded back to the original 12-bit DN. However there is an ambiguity when inverting, the 8-bit value could have been any of the 12-bit values within the particular bin. Simply inverted equation returns the lowest 12-bit DN within the bin. An alternate method is to use a lookup table and for a particular implementation the analyst can choose the lowest, middle, or highest value within a bin (or any value that meets the particular requirements).

References

C.W. Allen, *Astrophysical Quantities*, 3rd edn. (The Athlone Press, London, 1976)

T. Becker, L. Weller, L. Gaddis, D. Soltesz, D. Cook, A. Bennett, D. Galuszka, B. Redding, J. Richie, Progress on reviving Lunar Orbiter: scanning, archiving, and cartographic processing at USGS, in *Lunar Planet. Sci. Conf. XXXV. Abstract 1791* (Lunar and Planetary Institute, Houston, 2004), CD-ROM

J.F. Bell III, M.J. Wollf, M.C. Malin, W.M. Calvin, B.A. Cantor, M.A. Caplinger, R.T. Clancy, K.S. Edgett, L.J. Edwards, J. Fahle, F. Ghaemi, R.M. Haberle, A. Hale, P.B. James, S.W. Lee, T. McConnochie, E. Noe Dobrea, M.A. Ravine, D. Schaeffer, K.D. Supulver, P.C. Thomas, Mars Reconnaissance Orbiter Mars Color Imager (MARCI): instrument description, calibration, and performance. J. Geophys. Res. **114**, E08S92 (2009). doi:10.1029/2008JE003315

D.T. Blewett, B.R. Hawke, P.G. Lucey, G.J. Taylor, R. Jaumann, P.D. Spudis, Remote sensing and geologic studies of the Schiller-Schickard region of the Moon. J. Geophys. Res. **100**, 16959–16978 (1995)

D.E. Bowker, J.K. Hughes, *Lunar Orbiter Photographic Atlas of the Moon*. NASA Special Publication, vol. 206 (1971)

D.B.J. Bussey, P.D. Spudis, M.S. Robinson, Illumination conditions at the lunar South Pole. Geophys. Res. Lett. **26**, 1187–1190 (1999)

E.N. Cameron, *Evaluation of the Regolith of Mare Tranquillitatis as a Source of Volatile Elements* (University of Wisconsin-Madison, Madison, 1993)

W.S. Cameron, G.J. Coyle, An analysis of the distribution of boulders in the vicinity of small lunar craters. Earth Moon Planets **3**, 159–188 (1971)
W.D. Carrier, G.R. Olhoeft, W. Mendell, Physical properties of the lunar surface, in *Lunar Sourcebook*, ed. by G.H. Heiken, D.T. Vaniman, B.M. French (Cambridge University Press, Cambridge, 1991), pp. 475–594
G. Chin, S. Brylow, M. Foote, J. Garvin, J. Kasper, J. Keller, M. Litvak, I. Mitrofanov, D. Paige, K. Raney, M. Robinson, A. Sanin, D. Smith, H. Spence, P. Spudis, S.A. Stern, M. Zuber, Lunar Reconnaissance Orbiter overview: the instrument suite and mission. Space Sci. Rev. **129**, 391–419 (2007)
M.J. Cintala, J.B. Garvin, S.J. Wetzel, The distribution of blocks around a fresh lunar mare crater, in *Lunar Planet. Sci. Conf. XIII* (Lunar and Planetary Institute, Houston, 1982), pp. 100–101
M.J. Cintala, K. McBride, Block distribution on the lunar surface: a comparison between measurements obtained from surface and orbital photography. NASA, Johnson Space Center, Houston, TX, 1995
C.R. Coombs, B.R. Hawke, A search for intact lava tubes on the Moon: Possible lunar base habitats, in Lunar and Planetary Institute, Houston, TX (1992), pp. 219–229
B.M. Cudnik, D.W. Palmer, D.M. Palmer, A. Cook, R. Venable, P.S. Gural, The observation and characterization of lunar meteoroid impact phenomena. Earth Moon Planets **93**, 97–106 (2003)
M.E. Davies, T.R. Colvin, M.J.S. Belton, J. Veverka, P.C. Thomas, The direction of the north pole and the control network of asteroid 951 Gaspra. Icarus **107**, 18–22 (1994)
F.K. Duennebier, Y. Nakamura, G.V. Latham, H.J. Dorman, Meteoroid storms detected on the Moon. Science **192**, 1000–1002 (1976)
F. El-Baz, L.J. Kosofsky, *The Moon as Viewed by Lunar Orbiter*. NASA SP (United States Government Printing Office (USGPO), Washington, 1970)
W.C. Feldman, D.J. Lawrence, R.C. Elphic, B.L. Barraclough, S. Maurice, I. Getenay, Polar hydrogen deposits on the Moon. J. Geophys. Res. **105**, 4175–4195 (2000)
L.R. Gaddis, C.M. Pieters, B. Ray Hawke, Remote sensing of lunar pyroclastic mantling deposits. Icarus **61**, 461–489 (1985)
L.R. Gaddis, A.S. McEwen, T.L. Becker, Compositional variations on the Moon: recalibration of Galileo solid-state imaging data for the Orientale region and farside. J. Geophys. Res. **100**, 26345–26356 (1995)
L.R. Gaddis, B.R. Hawke, M.S. Robinson, C. Coombs, Compositional analyses of small lunar pyroclastic deposits using Clementine multispectral data. J. Geophys. Res. **105**, 4245–4262 (2000)
L. Gaddis, M.I. Staid, A. Tyburczy, B.R. Hawke, N.E. Petro, Compositional analyses of lunar pyroclastic deposits. Icarus **161**, 262–280 (2003)
D.E. Gault, Saturation and equilibrium conditions for impact cratering on the lunar surface: criteria and implications. Radio Sci. **5**, 273–291 (1970)
A.W. Gifford, F. El-Baz, Thicknesses of lunar mare flow fronts. Moon Planets **24**, 391–398 (1981)
T.A. Giguere, B.R. Hawke, D.T. Blewett, D.B.J. Bussey, P.G. Lucey, G.A. Smith, P.D. Spudis, G.J. Taylor, Remote sensing studies of the Lomonosov-Fleming region of the Moon. J. Geophys. Res. **108**, 5118 (2003)
T.A. Giguere, B.R. Hawke, D.T. Blewett, B.A. Campbell, J.J. Gillis-Davis, P.G. Lucey, C.A. Peterson, C. Runyon, G.J. Taylor, *Cryptomare and Pyroclastic Deposits in the Gassendi Region of the Moon* (2007), p. 1132
R. Goddard, in *The Papers of Robert H. Goddard*, ed. by E.C. Goddard, G.E. Pendray (McGraw-Hill, New York, 1920), pp. 413–430
R.O. Green, C. Pieters, P. Mouroulis, G. Sellars, M. Eastwood, S. Geier, J. Shea, The Moon mineralogy mapper: characteristics and early laboratory calibration results, in *Lunar Planet. Sci. Conf. XXXVIII*, Abstract 2354 (Lunar and Planetary Institute, Houston, 2007), CD-ROM
B. Hapke, *Theory of Reflectance and Emittance Spectroscopy* (Cambridge University Press, Cambridge, 1993)
J. Haruyama, T. Matsunaga, M. Ohtake, T. Morota, C. Honda, Y. Yokota, M. Torii, Y. Ogawa, LISM Working Group, Global lunar surface mapping experiment using the Lunar Imager/Spectrometer on Selene. Earth Planets Space **60**, 243–256 (2008)
B.R. Hawke, J.J. Gillis, T.A. Giguere, D.T. Blewett, D.J. Lawrence, P.G. Lucey, G.A. Smith, P.D. Spudis, G.J. Taylor, *Remote Sensing and Geologic Studies of the Balmer Region of the Moon* (2004), p. 1190
B.R. Hawke, J.J. Gillis, T.A. Giguere, D.T. Blewett, D.J. Lawrence, P.G. Lucey, G.A. Smith, P.D. Spudis, G.J. Taylor, Remote sensing and geologic studies of the Balmer-Kapteyn region of the Moon. J. Geophys. Res. **110**, E06004 (2005)
B.R. Hawke, T.A. Giguere, D.T. Blewett, B.A. Campbell, J.J. Gillis-Davis, J.J. Hagerty, D.J. Lawrence, P.G. Lucey, C.A. Peterson, G.A. Smith, P.D. Spudis, G.J. Taylor, *Remote Sensing Studies of the Schiller-Schickard Region of the Moon: Final Results* (2007), p. 1474
B.R. Hawke, T.A. Giguere, D.T. Blewett, J.M. Boyce, J.J. Gillis-Davis, J.J. Hagerty, P.G. Lucey, C.A. Peterson, G.A. Smith, P.D. Spudis, G.J. Taylor, *Light Plains and Cryptomare Deposits on the Northeastern Portion of the Lunar Nearside* (2008), p. 1512

J.W. Head, T.B. McCord, Imbrian-age highland volcanism on the Moon: the Gruithuisen and Mairan Domes. Science **199**, 1433–1436 (1978)
G.H. Heiken, D.T. Vaniman, B.M. French (eds.), *Lunar Sourcebook* (Cambridge University Press, Cambridge, 1991)
H. Hiesinger, J.W. Head, U. Wolf, R. Jaumann, G. Neukem, Ages and stratigraphy of mare basalts in Oceanus Procellarum, Mare Nubium, Mare Cognitum, and Mare Insularum. J. Geophys. Res. **108**, 5065 (2003)
A.P. Ingersoll, T. Svitek, B.C. Murray, Stability of polar frosts in spherical bowl-shaped craters on the Moon, Mercury, and Mars. Icarus **100**, 40–47 (1992)
B.A. Ivanov, Earth/Moon impact rate comparisons: Searching constraints for lunar secondary/primary cratering proportion. Icarus **183**, 504–507 (2006)
J.R. Janesick, *Photon Transfer*. SPIE Publications (2007)
JMars (2010). http://jmars.asu.edu/node/2055
S.J. Lawrence, M.S. Robinson, M. Broxton, J.D. Stopar, W. Close, J. Grunsfeld, R. Ingram, L. Jefferson, S. Locke, R. Mitchell, T. Scarsella, M. White, M.A. Hager, T.R. Watters, E. Bowman-Cisneros, J. Danton, J. Garvin, The Apollo digital image archive: new research and data products. LPI Contrib. **1415**, 2066 (2008a)
S.J. Lawrence, B.R. Hawke, J.J. Gillis-Davis, G.J. Taylor, D.J. Lawrence, J.T. Cahill, J.J. Hagerty, P.G. Lucey, G.A. Smith, K. Keil, Composition and origin of the Dewar geochemical anomaly. J. Geophys. Res. (Planets) **113**, 02001 (2008b)
S.W. Lee, P. Thomas, J. Veverka, Phobos, Deimos, and the Moon: size and distribution of crater ejecta blocks. Icarus **68**, 77–86 (1986)
M.C. Malin, J.F. Bell III, W. Calvin, R.T. Clancy, R.M. Haberle, P.B. James, S.W. Lee, P.C. Thomas, M.A. Caplinger, Mars Color Imager (MARCI) on the Mars Climate Orbiter. J. Geophys. Res. **106**, 17651–17672 (2001)
M.C. Malin, J.F. Bell III, W.M. Calvin, B.A. Cantor, M.A. Caplinger, R.T. Clancy, T. Ghaemi, R.M. Haberle, P.B. James, S.W. Lee, T. McConnochie, E.N. Dobrea, M.A. Ravine, P.C. Thomas, M.J. Wolff, Mars Reconnaissance Orbiter Mars Color Imager (MARCI) and Context Camera (CTX) pre-flight calibration report [MSSS-CTX-DOC-2002]. Malin Space Science Systems, San Diego, CA, 2005
M.C. Malin, J.F. Bell, B.A. Cantor, M.A. Caplinger, W.M. Calvin, R.T. Clancy, K.S. Edgett, L. Edwards, R.M. Haberle, P.B. James, S.W. Lee, M.A. Ravine, P.C. Thomas, M.J. Wolff, Context camera investigation on board the Mars Reconnaissance Orbiter. J. Geophys. Res. **112**, E05S04 (2007)
H. Masursky, G.W. Colton, F. El-Baz (eds.), *Apollo over the Moon: A View From Orbit*. NASA SP, vol. 362 (United States Government Printing Office, Washington, 1978)
M. Minnaert, Photometry of the Moon, in *Planets and Satellites*, ed. by G.P. Kuiper, B.M. Middlehurst (University of Chicago Press, Chicago, 1961), p. 601
H.J. Moore, Large blocks around lunar craters, in *Analysis of Apollo 10 Photography and Visual Observations* (National Aeronautics and Space Administration, Washington, 1971), pp. 26–27
R.G. Musgrove, *Lunar Photographs from Apollos 8, 10, and 11*. NASA Special Publication, vol. 246 (1971)
NASA, *A Site Selection Strategy for a Lunar Outpost: Science and Operational Parameters* (Lunar and Mars Exporation Program Office, Johnson Space Center, Houston, 1990)
NASA, *The Vision for Space Exploration [NP-2004-01-334-HQ]* (NASA, Washington, 2004a)
NASA, Announcement of opportunity Lunar Reconnaissance Orbiter measurement investigations. NNH04ZSS003O, 2004b
NASA, Exploration systems architecture study. NASA-TM-2005-214062, 2005
H. Noda, H. Araki, S. Goossens, Y. Ishihara, K. Matsumoto, S. Tazawa, N. Kawano, S. Sasaki, Illumination conditions at the lunar polar regions by KAGUYA(SELENE) laser altimeter. Geophys. Res. Lett. **35**, L24203 (2008)
S. Nozette, P. Rustan, L.P. Pleasance, D.M. Horan, P. Regeon, E.M. Shoemaker, P.D. Spudis, C.H. Acton, D.N. Baker, J.E. Blamont, B.J. Buratti, M.P. Corson, M.E. Davies, T. Duxbury, E.M. Eliason, B.M. Jakosky, J.F. Kordas, I.T. Lewis, C.L. Lichtenberg, P.G. Lucey, E. Malaret, M.A. Massie, J.H. Resnick, C.J. Rollins, H.S. Park, A.S. McEwen, R.E. Priest, C. Pieters, R.A. Reisse, M.S. Robinson, R.A. Simpson, D.E. Smith, T.C. Sorensen, R.W. Vorder Breugge, M.T. Zuber, The Clementine mission to the Moon: scientific overview. Science **266**, 1835–1839 (1994)
S. Nozette, P.D. Spudis, M.S. Robinson, D.B.J. Bussey, C. Lichenstein, R. Bonner, Integration of lunar polar remote-sensing data sets: evidence for ice at the lunar south pole. J. Geophys. Res. **106**, 23253–23266 (2001)
V.R. Oberbeck, W.L. Quaide, Estimated thickness of a fragmental surface layer of Oceanus Procellarum. J. Geophys. Res. **72**, 4697–4704 (1967)
V.R. Oberbeck, W.L. Quaide, Genetic implications of Lunar regolith thickness variations. Icarus **9**, 446–465 (1968)

J.L. Ortiz, P.V. Sada, L.R. Bellot Rubio, F.J. Aceituno, J. Aceituno, P.J. Gutierrez, U. Thiele, Optical detection of meteoroidal impacts on the Moon. Nature **405**, 921–923 (2000)
J.L. Ortiz, J.A. Quesada, J. Aceituno, F.J. Aceituno, L.R.B. Rubio, Observation and interpretation of Leonid impact flashes on the Moon in 2001. Astrophys. J. **576**, 567–573 (2002)
J. Ortiz, F. Aceituno, J. Quesada, J. Aceituno, M. Fernández, P. Santos-Sanz, J. Trigo-Rodríguez, J. Llorca, F. Martín-Torres, P. Montañés-Rodríguez, E. Pallé, Detection of sporadic impact flashes on the Moon: Implications for the luminous efficiency of hypervelocity impacts and derived terrestrial impact rates. Icarus **184**, 319–326 (2006)
W.L. Quaide, V.R. Oberbeck, Thickness determinations of the lunar surface layer from lunar impact craters. J. Geophys. Res. **73**, 5247–5270 (1968)
D. Stoffler, G. Ryder, B.A. Ivanov, N.A. Artemieva, M.J. Cintala, R.A.F. Grieve, Cratering history and lunar chronology. Rev. Min. Geochem. **60**, 519–596 (2006)
G.J. Taylor, P.D. Spudis, Geoscience and a Lunar Base: A Comprehensive Plan for Lunar Exploration, 1990
USGS, 2010. http://isis.astrogeology.usgs.gov/UserDocs/index.html
J.K. Wagner, B.W. Hapke, E.N. Wells, Atlas of reflectance spectra of terrestrial, lunar, and meteoritic powders and frosts from 92 to 1800 nm. Icarus **69**, 14–28 (1987)
K. Watson, B.C. Murray, H. Brown, On the possible presence of ice on the Moon. J. Geophys. Res. **66**, 1598–1600 (1961)
D.E. Wilhelms, *Stratigraphy of Part of the Lunar Near Side*. United States Geological Survey Professional Paper, vol. 1046-A (United States Government Printing Office, Washington, 1980)
D.E. Wilhelms, J.F. McCauley, N.J. Trask, *The Geologic History of the Moon*. U.S. Geol. Surv. Prof. Pap., vol. 1348 (United States Government Printing Office, Washington, 1987)
R.J. Williams, D.S. McKay, D. Giles, T.E. Bunch, Mining and beneficiation of lunar ores, in *Space Resources and Space Settlements*, ed. by G.K. O'Neill, J. Billingham, W. Gilbreath, B. O'Leary (NASA, 1979), pp. 275–188
C.A. Wood, *Lunar Concentric Craters* (1978), pp. 1264–1266
C.A. Wood, J.W. Head, Geologic setting and provenance of spectrally distinct pre-mare material of possible volcanic origin, in *LPI Contributions* (Lunar Science Institute, Houston, 1975), p. 189
M. Yanagisawa, N. Kisaichi, Lightcurves of 1999 Leonid impact flashes on the Moon. Icarus **159**, 31–38 (2002)
Y. Zhao, F. Shadman, Production of oxygen from lunar ilmenite, in *Resources of Near-Earth Space*, ed. by J. Lewis, M.S. Matthews, M.L. Guerrieri (University of Arizona Press, Tucson, 1993), pp. 149–178